

MASTER'S THESIS

DESIGN AND PERFORMANCE EVALUATION OF A LOW-MASS
IN-BEAM CHARGED PARTICLE DETECTOR FOR THE KOTO
EXPERIMENT AT J-PARC

Taylor Cassidy Nunes

Fall 2021

Osaka University

Graduate School of Science

Department of Physics

Taku Yamanaka Lab

Contents

1	Introduction	2
1.1	Overview of the KOTO Experiment	2
1.1.1	Physics Motivation	2
1.1.2	Concept of Signal Measurement	2
1.2	The KOTO Experiment	2
1.2.1	Beamline	2
1.2.2	Detector Principle	4
1.2.3	Detector	5
1.3	Charged Kaon Background	6
1.4	Prototype Charged Veto Detector	6
1.4.1	Purpose	6
1.4.2	Design	6
1.4.3	Limitations	7
1.5	Purpose of This Study	8
2	Upstream Charged Veto Detector Design	9
2.1	Requirements	9
2.2	Overall Design	9
2.3	Charged Particle Detection Mechanism	11
2.3.1	Scintillation Fibers	11
2.3.2	MPPCs	12
2.4	Mechanics	12
2.4.1	Support Structure	12
2.4.2	Changeable Angle	14
2.4.3	MPPC Fixture	15
2.4.4	Core and Halo Separation	16
2.5	Electronics	18
2.5.1	Signal Readout	18
2.5.2	LED	18

2.6	Replacement of MPPCs	19
3	Performance Test	20
3.1	Purpose	20
3.2	Experimental Setup	20
3.3	Peak Detection method	21
3.4	Light Yield	21
3.5	Inefficiency Measurement	23
3.5.1	Overview of Inefficiency	23
3.5.2	Sources of Inefficiency	24
3.5.3	Angle Scan	24
3.5.4	Position Scan	26
4	Estimation of Accidental Loss	28
4.1	Overview of Accidental Loss	28
4.1.1	Definition of accidental loss	28
4.1.2	Target for UCV	28
4.2	Method to Simulate Data	28
4.2.1	Selection of method	28
4.2.2	Waveform simulation	29
4.2.3	MPPC Crosstalk	30
4.3	Dark Current	31
4.3.1	Rate Calculation	31
4.3.2	Irradiation Effect	31
4.4	Beam Particles	32
4.4.1	Mechanism	32
4.4.2	Geant4 Simulation	32
4.4.3	Beam Normalization	32
4.5	Expected Accidental Loss	33
4.5.1	Calculation of accidental loss	33
4.5.2	Dark Current	33
4.5.3	Beam particles	34
4.6	Threshold and Angle Selection	34
5	Functionality at J-PARC	36
5.1	Installation	36
5.2	Beam Test Comparison	36
5.3	Beam Coverage	36
5.4	Accidental Loss	39

5.4.1	Data Selection	39
5.4.2	Calculation method	39
5.4.3	Comparison to Simulation	40
5.5	Inefficiency	40
5.5.1	Charged Kaon Reconstruction	40
5.5.2	Charged Kaon Selection criteria	43
5.5.3	Comparison to Electron Beam Data	43
6	Impact of Upstream Charged Veto	45
6.1	Accidental Loss	45
6.2	Background Reduction	45
7	Discussion	47
7.1	Longevity of MPPCs	47
7.2	Accidental Loss Calculation Method	47
8	Conclusion	49

Abstract

The KOTO experiment is studying CP violation by searching for the rare decay of $K_L \rightarrow \pi^0 \nu \bar{\nu}$ at J-PARC. The branching ratio predicted by the standard model is 3.0×10^{-11} and the KOTO experiment plans to achieve a sensitivity on the same order. In the analysis of data taken in 2016-2018 the largest background to $K_L \rightarrow \pi^0 \nu \bar{\nu}$ came from the decay of charged kaons in the beam. To distinguish these events a charged particle detector was designed from scintillation fibers and photosensitive electronics and was installed in the beam at the upstream edge of the KOTO detector. This study focuses on the mechanical design of the detector and its resulting performance.

A prototype version was designed in 2019 and tested in 2020. The detector in this study was improved from the prototype by being thinner, more noise resistant, and having larger coverage. It was also designed to have a changeable angle relative to beam to reduce inefficiency. Using an electron beam its functionality was confirmed and its inefficiency was measured. The negative impact on the sensitivity of the KOTO experiment was simulated and, along with the measured inefficiency, was used to determine the angle of the detector before installation at J-PARC. After installation, the detector performance was analyzed with accelerator beam data. During the run in spring 2021, it was able to reduce the charged kaon background by 96%.

Chapter 1

Introduction

1.1 Overview of the KOTO Experiment

1.1.1 Physics Motivation

The universe that exists today has a large unbalance between matter and antimatter. First published by Andrei Sakharov in 1967 [9], one of the necessary conditions for the asymmetric formation of matter and antimatter is CP violation. Predicted by the standard model is rare CP violating decay mode of the long lived neutral kaon, $K_L \rightarrow \pi^0 \nu \bar{\nu}$. The KOTO experiment is searching for $K_L \rightarrow \pi^0 \nu \bar{\nu}$. Experiments have yet to achieve a sensitivity to it on the same order as the branching ratio predicted by the standard model, 3.0×10^{-11} [1]. If the measured decay differs from the prediction, there may be new physics that can help better understand CP violation. The aim of the KOTO experiment is to achieve a sensitivity of $\mathcal{O}(10^{-11})$. The current upper limit for the branching ratio of $K_L \rightarrow \pi^0 \nu \bar{\nu}$ was set by KOTO in 2015 at 3.0×10^{-9} at the 90% confidence level [1].

1.1.2 Concept of Signal Measurement

The signature of the $K_L \rightarrow \pi^0 \nu \bar{\nu}$ decay are 2γ from the decay of π^0 and nothing because the neutrinos are undetectable. To detect the 2γ , the KOTO detector uses an electromagnetic calorimeter located downstream from the K_L decay region. To measure the absence of all other particles, hermetic veto detectors surround the decay region. The $K_L \rightarrow \pi^0 \nu \bar{\nu}$ decay is shown in Fig. 1.1

1.2 The KOTO Experiment

1.2.1 Beamline

The KOTO experiment is located at the Japan Proton Accelerator Research Complex (J-PARC) in Tokai Village in Ibaraki Japan. As shown in Fig. 1.2, the facility consists of three accelerators, the Linac, the Rapid-cycle Synchrotron (RCS), and the Main Ring (MR). Through these three accelerators, protons are generated and brought up to 30 GeV. They are then extracted from MR into Hadron Hall where the KOTO detector is located.

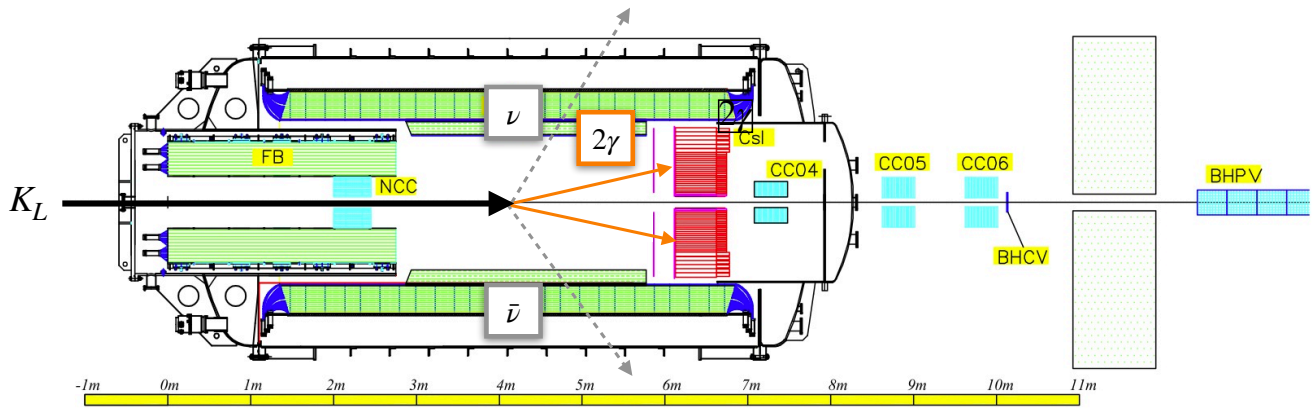


Figure 1.1: Decay of $K_L \rightarrow \pi^0 \nu \bar{\nu}$ in the KOTO detector.

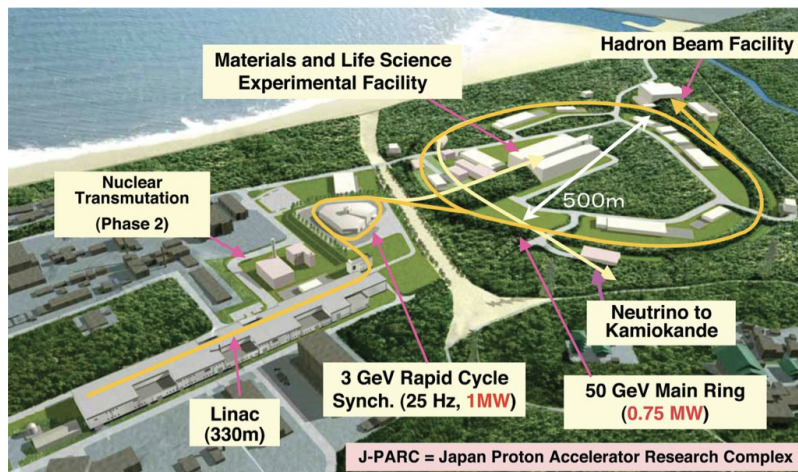


Figure 1.2: The J-PARC facility [5].

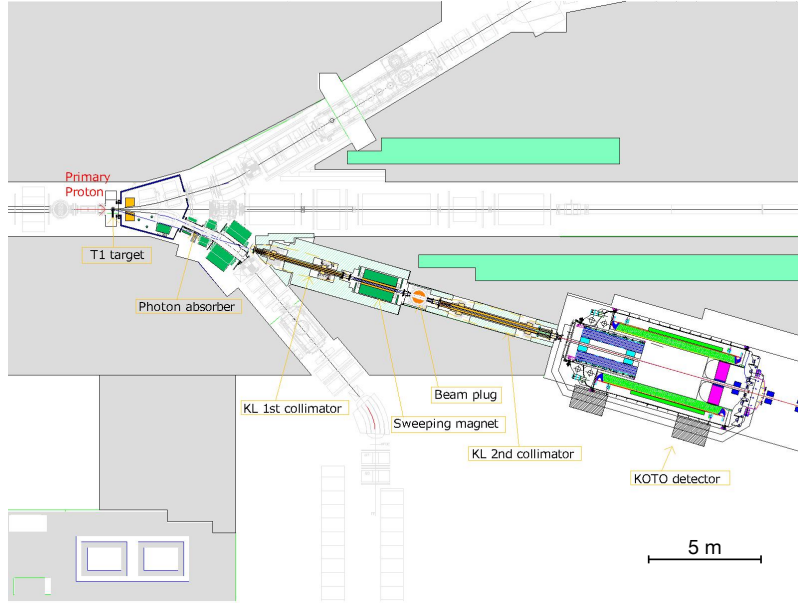


Figure 1.3: Schematic of extraction between gold target and the KOTO detector.

After being extracted to Hadron Hall the protons are incident on a gold target. The secondary particles produced at the target are transported to the KOTO experiment over the course of 20 m to eliminate short-lived particles. The particles pass through a photon absorber, two collimators to narrow the beam, and a 1.2-T sweeping magnet to remove charged particles, as shown in Fig. 1.3. The particles pass through a closable beam plug before the second collimator.

To assist in analysis, the KOTO collaboration has simulated the momentum, position, and flux of particles entering the detector from the beamline. This is done by using a Geant3 simulation of the target, collimators, and lead absorber and is referred to as the KOTO beamline simulation. Neutrons and photons are the most prevalent particles in the beam at the entrance of the detector. At a beam power of 50 kW, the incident rate for each is 160 MHz and 280 MHz, respectively.

1.2.2 Detector Principle

The veto detectors measure signal from all other sources that are not the $K_L \rightarrow \pi^0 \nu \bar{\nu}$ decay. This includes additional particles in the beam, other decay modes of K_L , and other backgrounds. The signals from veto detectors are analyzed, and for each event if any veto detectors contain a signal, the event is excluded as a candidate for $K_L \rightarrow \pi^0 \nu \bar{\nu}$, hence the name veto.

A true $K_L \rightarrow \pi^0 \nu \bar{\nu}$ decay produces no signal in veto detectors; however, signal can still be measured due to noise or accidental particles, causing that event to be vetoed. The fraction of true $K_L \rightarrow \pi^0 \nu \bar{\nu}$ decays that we veto, is referred to as the accidental loss and needs to be minimized to increase sensitivity.

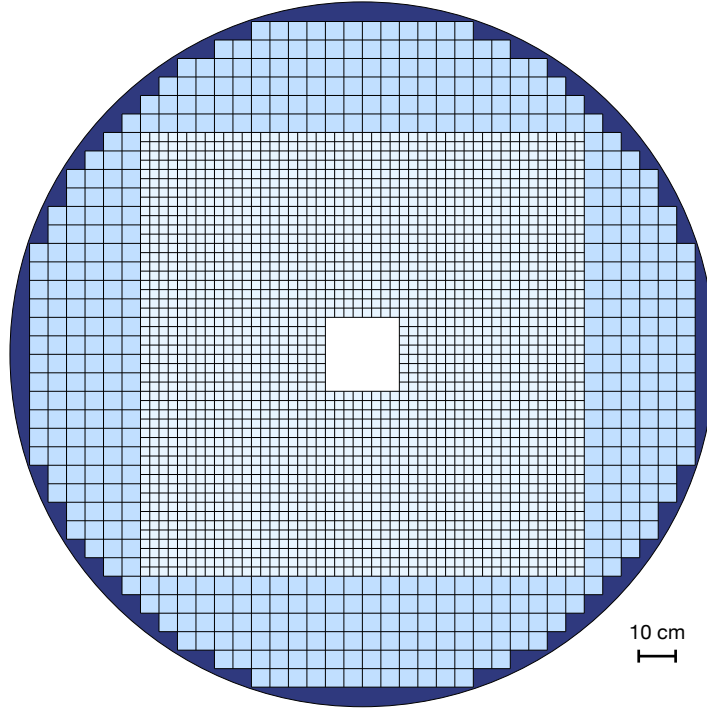


Figure 1.4: The cross-section of CSI.

1.2.3 Detector

The KOTO detector is defined in a right-handed coordinate system with the $+z$ -direction defined as the downstream direction of the beam and the y -direction as vertically up with the origin at the front end surface of the KOTO detector centered in the beam. The main component of the KOTO experiment is a two-meter-diameter cylindrical electromagnetic calorimeter (CSI) made from scintillating undoped cesium iodide crystals as shown in Fig. 1.4 [10]. The CSI has a $15\text{ cm} \times 15\text{ cm}$ beamhole located in the center to allow for the passage of remaining beam particles. The scintillation light is read out from the crystals by photomultiplier tubes (PMT) on the downstream end and multi-pixel photon counters (MPPC) on the upstream end. A photon or charged particle that is incident on CSI will deposit energy across multiple crystals. The group of crystals with energy deposited in them is referred to as a cluster. Neutrons will also deposit energy through hadronic interactions.

Sitting in front of CSI is a charged veto detector (CV). The CV is made of two planes of wavelength-shifting scintillation counters read out by MPPCs [6]. For particles that enter CSI, CV provides a method to distinguish between charged particles and neutral particles. Additional veto detectors hermetically surrounds the KOTO detector.

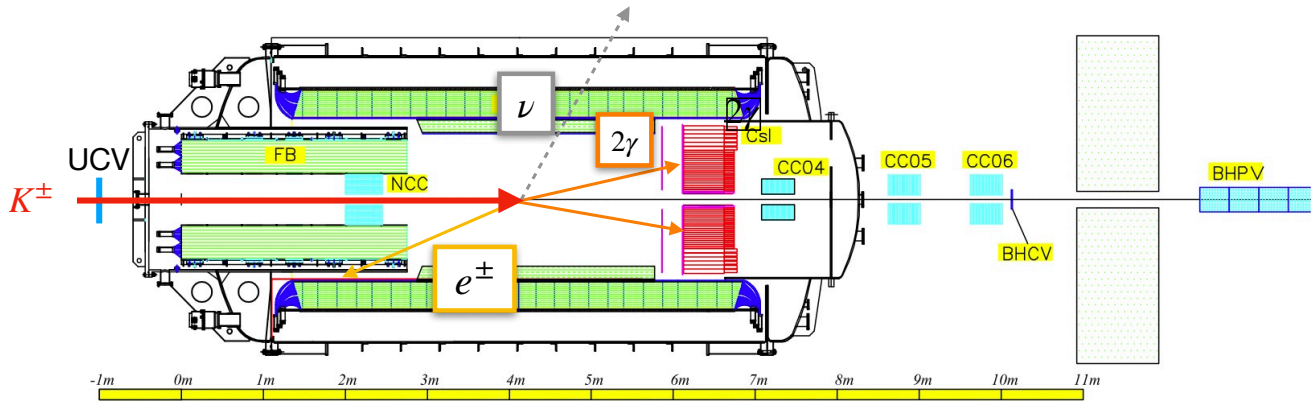


Figure 1.5: Charged kaon decay as a background.

1.3 Charged Kaon Background

One background for the KOTO experiment comes from the decay of charged kaons. When a K_L scatters at the photon absorber and hits a collimator, charge exchange can occur where K^\pm is produced. If the K^\pm decays by $K^\pm \rightarrow \pi^0 e^\pm \nu$ and the e^\pm hits dead material in the detector, as shown in Fig. 1.5, the 2γ from the π^0 will mimic the signal from $K_L \rightarrow \pi^0 \nu \bar{\nu}$.

In the 2016-2018 data set, the largest data set taken since the start in 2013, charged kaon decays were the largest background. After all cuts were applied, the expected number of events from this background was 0.87 ± 0.25 events [2]¹.

1.4 Prototype Charged Veto Detector

1.4.1 Purpose

To detect charged kaons in the beam for vetoing in analysis and to confirm our calculated number of K^\pm , a prototype detector was designed and installed in 2019. It was installed at the upstream edge of the KOTO detector and hence is called the prototype upstream charged veto. The prototype was designed to last one run measured the feasibility of an upstream charged veto.

1.4.2 Design

The detector needed to provide an output signal that is easily discernible from noise. For charged particles, one method to produce a signal is with scintillation material. The scintillation material emits light under interaction with charged particles which can then be read out by photosensitive devices. Since the detector sits in the beam and can interact with beam particles, it can cause scattering of particles from their original trajectory, leading to accidental loss in other detectors and an increase in backgrounds. To avoid this the amount of material in contact with the beam, referred to as the material budget, needs to be reduced.

¹The corresponding expected number of standard model events for $K_L \rightarrow \pi^0 \nu \bar{\nu}$ is 0.04.

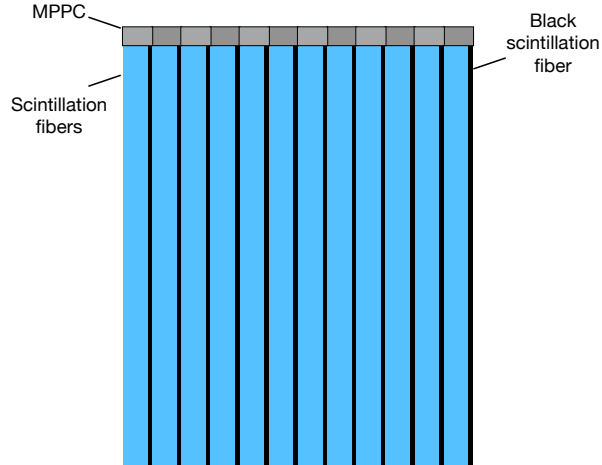


Figure 1.6: Prototype upstream charged veto detector.

The prototype detector used $1\text{ mm} \times 1\text{ mm}$ square scintillation fibers to detect particles. The fibers consist of a core scintillation material surrounded by a cladding. The cladding provides a difference in refractive index between the inside and the outside, allowing for light to travel to the end by total internal reflection. Eighty-four 100-mm-long scintillation fibers were arranged in a plane. Fibers were grouped into units of seven and read out with $6\text{ mm} \times 6\text{ mm}$ photosensitive-area MPPCs from Hamamatsu Electronics, as shown in Fig. 1.6. The majority of the prototype used Kuraray [8] produced fibers, but every seventh fiber was from Saint-Gobain.

The prototype upstream charged veto was effective as a proof of concept for an upstream charged veto. It was used in conjunction with K^\pm analysis in 2020 to confirm the K^\pm flux. The ratio of K^\pm to K^L was $(2.6 \pm 0.1) \times 10^{-5}$ [2].

1.4.3 Limitations

The prototype achieved its goal but had the following limitations that needed to be improved for the next model.

As will be explained in Section 2.3.1, gaps between fibers produce paths for particles to travel where they do not interact with scintillation material and thus produce no signal. This gap effect resulted in a 7% inefficiency.

The prototype had a coverage in the x -direction of $\pm 42\text{ mm}$. The profile of charged kaons in the beam at the installation location, simulated by a member at Osaka University with the KOTO beamline simulation, is represented in Fig. 2.1 and has a width in the x -direction of $\pm 50\text{ mm}$. The limited coverage of the prototype caused 8% inefficiency.

Each unit of 7 fibers was read out by a 36 mm^2 photosensitive area, and therefore 81% of the photosensitive area was unused. Internal noise production in the MPPCs is proportional to the photosensitive area

due to an increase the amount of semiconductor material. The amount of irradiation is also proportional the photosensitive area due to more frequent hits from accidental particles. Reducing the photosensitive area increases the S/N ratio of the detector.

When using the prototype, the accidental loss in other detectors from scattered particles was increased by 12% from a study by Ryota Shiraishi. The background from the decay of non-beam-centered K_L due to scattering increased by a factor of 3.5 in a study by Yuya Noichi [7]. To minimize these effects the amount of material in the beam needs to be minimized further.

1.5 Purpose of This Study

Over the course of the later half of 2020 the students and staff in Yamanaka Group at Osaka university have designed and tested an upstream charged veto (UCV) to be the successor to the prototype. This study focuses on the mechanical design and development of the UCV and the evaluation of its performance. To test the inefficiency of the UCV, an electron test beam was used. To estimate the accidental loss, simulation was conducted. The results of both of these were compared to the performance after installation at J-PARC and, the impact on the KOTO experiment is discussed.

Chapter 2

Upstream Charged Veto Detector Design

2.1 Requirements

Since the primary purpose of the UCV is to veto the charged kaon background, the UCV must be sufficiently large to cover the charged kaon flux in both the x and the y directions. From the output of the standard KOTO beamline simulation, the x and y locations of charged kaons passing through the z position of the UCV had been previously estimated, as shown in Fig. 2.1. The charged kaon flux is well contained within ± 60 mm in both the x and y directions.

After deciding to design the UCV, a collaboration member designed a vacuum chamber to contain the UCV. The inner dimensions of the chamber are 520 mm, 360 mm, and 192 mm in the x , y , and z directions, respectively. The available space in the z direction for the UCV, however, is only 172 mm since 20 mm is reserved in the downstream portion of the chamber for an aluminum target¹.

The goal of the UCV is to have an inefficiency of less than 10% and to minimize the accidental loss to the order of 5%. A 10% inefficiency would allow for the reduction of the charged kaon background by one order of magnitude. The total accidental loss before 2021 due to all the other detectors was 53%, and 5% is significantly low to not drastically impact the total.

2.2 Overall Design

A charged veto detector was designed for installation in the upstream region of the KOTO detector. The design consists of a plane of 0.5 mm thick scintillation fibers, bundled in units of 16 whose scintillation light is measured by 3 mm \times 3 mm MPPCs as will be explained in Section 2.3. The resulting 12 channels are read out with 500-MHz analog to digital converters (ADC). Shown in Fig. 2.2 is the UCV after assembly.

¹The aluminum target is a removable target that sits in the beam and is used for enhancing neutron scattering to study background.

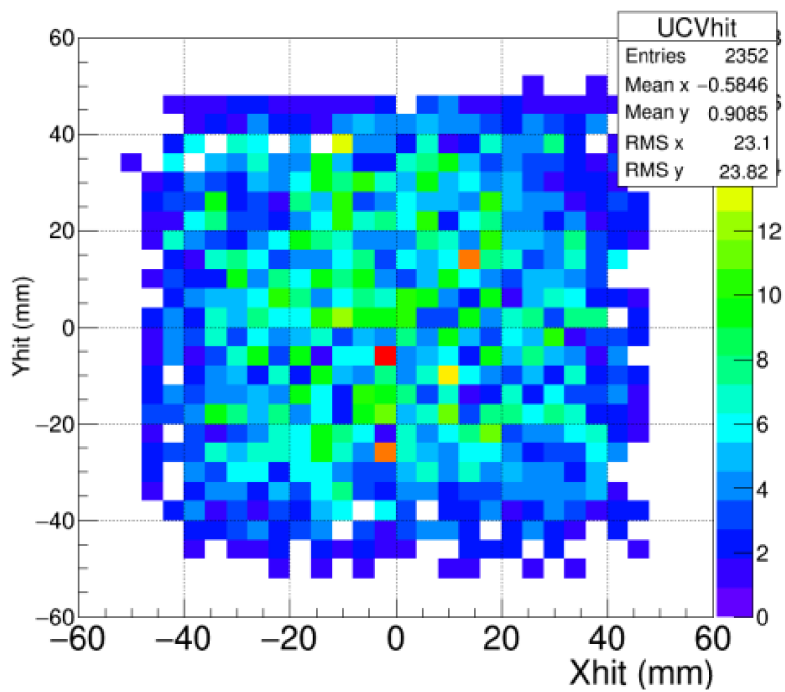


Figure 2.1: Geant4 hit distribution of charged kaons at the UCV z position.

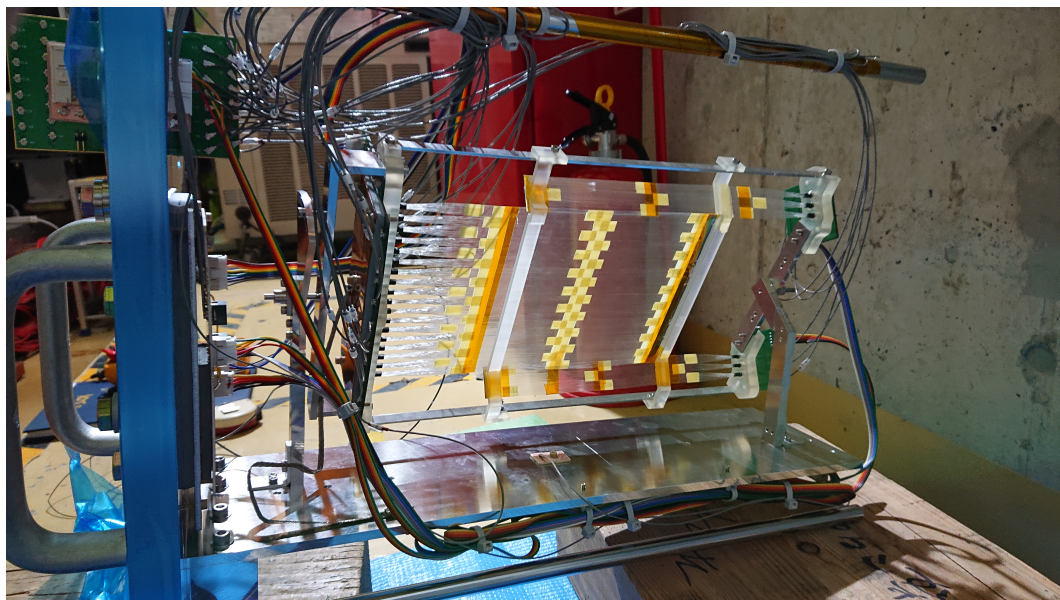


Figure 2.2: UCV after assembly on the flange.

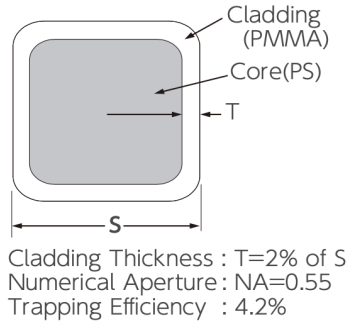


Figure 2.3: Scintillation fibers cross section [8].

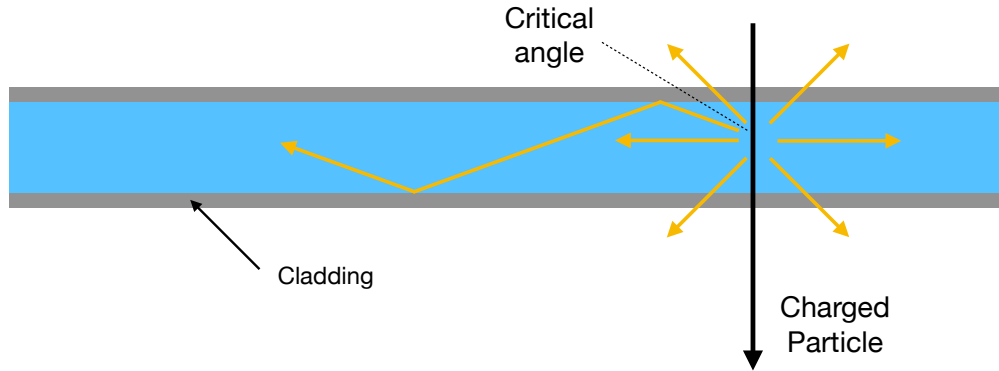


Figure 2.4: Scintillation fibers light production.

2.3 Charged Particle Detection Mechanism

2.3.1 Scintillation Fibers

The thickness of the scintillation fibers for the UCV was chosen to be 0.5 mm, half the thickness of those for the prototype. This was done to reduce the amount of material present in the beam. Fibers were selected to be $0.5 \text{ mm} \times 0.5 \text{ mm}$ SCSF-78 from Kuraray. Preliminary studies showed that 0.5 mm fibers resulted in a measurable light of $\mathcal{O}(10)$ photoelectrons. The fibers consist of a 0.48 mm thick scintillating polystyrene core and a 0.01 mm thick polymethylmethacrylate cladding as shown in Fig. 2.3.

Figure 2.4 shows the production of light from charged particles in scintillation fibers. As charged particles pass through the core, they electromagnetically interact with and excite electrons in the material. When the electrons de-excite, they release photons which travel down to the end of the fiber by means of total internal reflection. Due to the isotropic emission of the photons the fibers have a trapping efficiency of 4.2% [8]. Since MPPCs are located on a single end of each fiber, reflective foil was added to the other end in order to reflect photons back and increase the light yield.

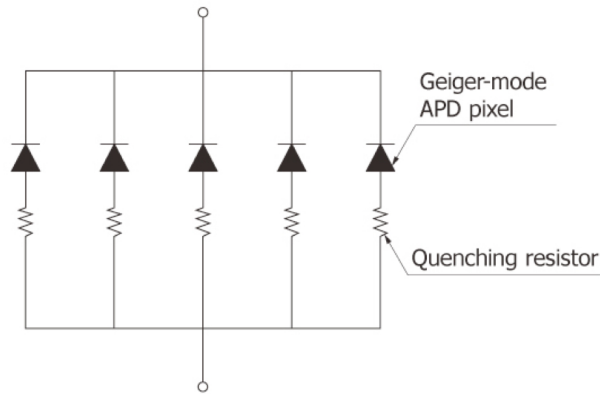


Figure 2.5: Internal schematic of an MPPC [3].

2.3.2 MPPCs

The photosensitive device to measure the light from the scintillation fibers was chosen to be $3\text{ mm} \times 3\text{ mm}$ S13360-3075CS MPPCs from Hamamatsu [4]. Compared to the prototype UCV, the photosensitive area is 4 times smaller, reducing the amount of incident neutrons and therefore the radiation damage.

An MPPC's photosensitive region is an array of pixels consisting of avalanche photodiodes (APD) and quenching resistors. This circuit is shown in Fig. 2.5. An APD is a silicon semiconductor with an applied bias voltage. When a photon with energy higher than the band gap energy is incident on an APD, an initial electron-hole pair is created (photoelectron). If the bias voltage is high enough, the electron and hole are accelerated by the internal electric field and collide with the crystal lattice generating an electron-hole-pair avalanche and thus creating a current. The current causes a high voltage drop across the quenching resistor and therefore lowers the bias voltage of the APD to below the avalanche threshold. The overall result is a short burst of a fixed quantity of current from one incident photon. If multiple pixels are hit at the same time, the resulting currents from each are summed [3].

Because of thermal excitation, MPPCs can produce single photoelectrons without any incident light. This is known as dark current, and increases with radiation damage.

MPPCs also suffer from crosstalk between pixels. During the avalanche process, an electron or hole has the possibility to emit its energy as a photon. The emitted photon can travel to a neighboring pixel and cause another avalanche. This can occur more than once in succession. Because of the short time in which this occurs, the output pulse of the MPPC is indistinguishable from that of multiple photon hits.

2.4 Mechanics

2.4.1 Support Structure

The support structure for the UCV consists of an aluminum base-plate fixed to the flange of the chamber as shown in Fig. 2.6. Attached to the top of the base-plate are two vertical aluminum supports to hold

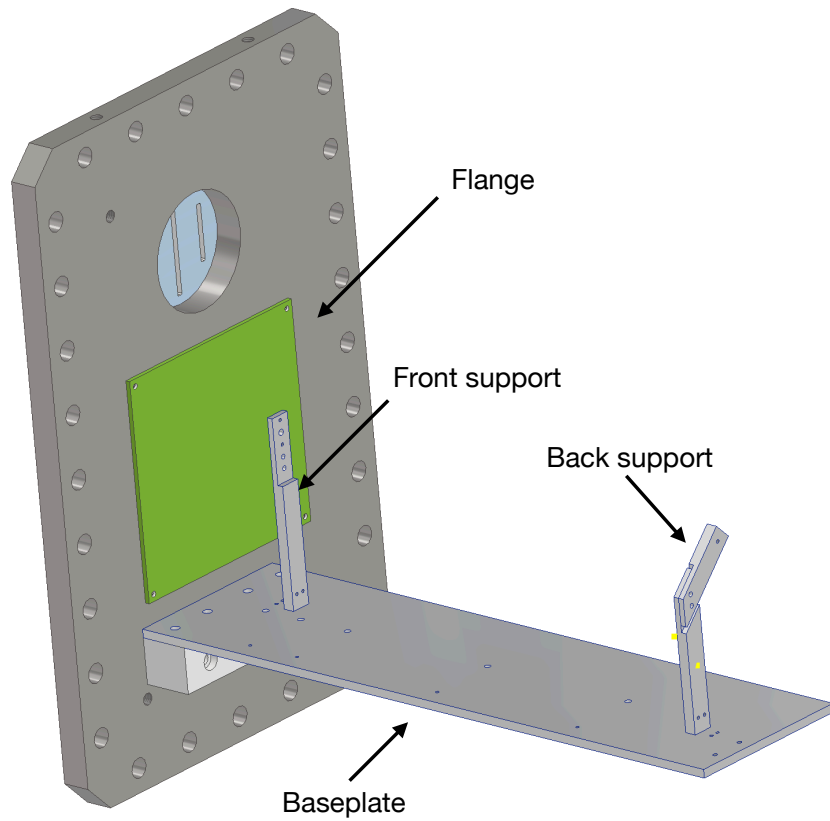


Figure 2.6: Flange and support structures.

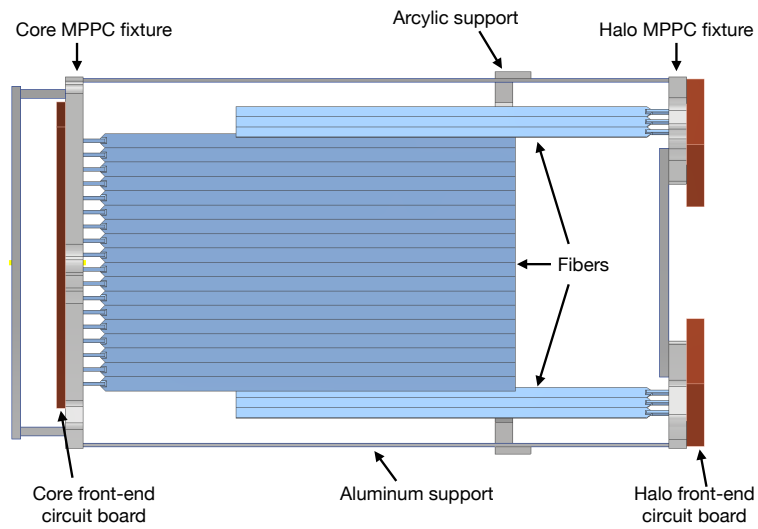


Figure 2.7: Inner frame to support the fibers, MPPCs, and front-end boards.

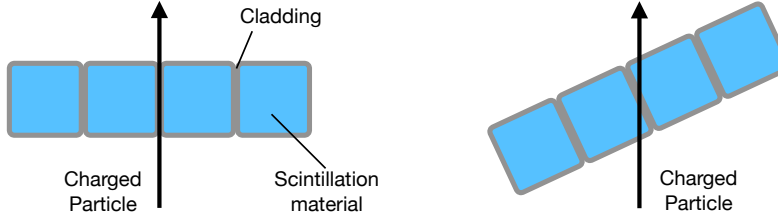


Figure 2.8: Particles passing through fibers at different angles.

the inner frame of the UCV. The support furthest from the flange (back support) is angled to prevent interference of the fibers.

As shown in Fig. 2.7, the inner frame of the UCV is a rigid support that contains the fibers, MPPCs, and front-end circuit boards. The aluminum support bars shown on the top and bottom provide connection between the MPPC holders on the right and left sides. This allows any stress to transfer through the aluminum and not through the fibers. Additional 3D printed acrylic supports, shown vertically in the middle, provide more stability to the fibers and help prevent them from bowing under gravity. The furthest left bar connects to a rotation shaft. Although the coverage of the UCV is ± 80 mm from the beam center in the x -direction, the inner frame was made larger, to position the MPPCs ± 170 mm away from the beam, thus decreasing the irradiation.

2.4.2 Changeable Angle

As discussed in Section 1.4.3, one of the limitations of the prototype UCV was the inefficiency due to the gap between the fibers. Since the core of the fiber is the only scintillating medium, the cladding effectively counts as a gap and results in detector inefficiency.

Shown in Fig. 2.8, when the direction of an incident particle is perpendicular to the plane of the UCV, the particle has a chance to travel through the gap without depositing energy. When the angle is offset from the perpendicular, however, the particle must come into contact with scintillation material.

Increasing the tilt of the UCV from perpendicular to the beam has additional effects. A larger angle provides a larger path length for the particle to travel and thus an increase in the light yield. The larger path length, however, also increases the material budget and can result in an increase in accidental loss or a production of backgrounds.

It was decided that the tilt would only need to vary between 0° and 45° , where 0° is perpendicular and 90° is parallel to the beam. The effect of the gap was expected to be overcome before 45° , and therefore further increase from 45° would not be necessary. To control the tilt, rotation shafts and shaft collars were added to both the front support and the back support to connect with the inner frame as shown in Fig. 2.9a and Fig. 2.9b. These shafts allow for the inner frame to rotate to any tilt. To constrain the angle between 0° and 45° an angular fixture containing bolt holes at 5° increments was added to the top of the front support as shown in Fig. 2.9c. The angle can be fixed with a bolt attached between the angular fixture and the inner frame.

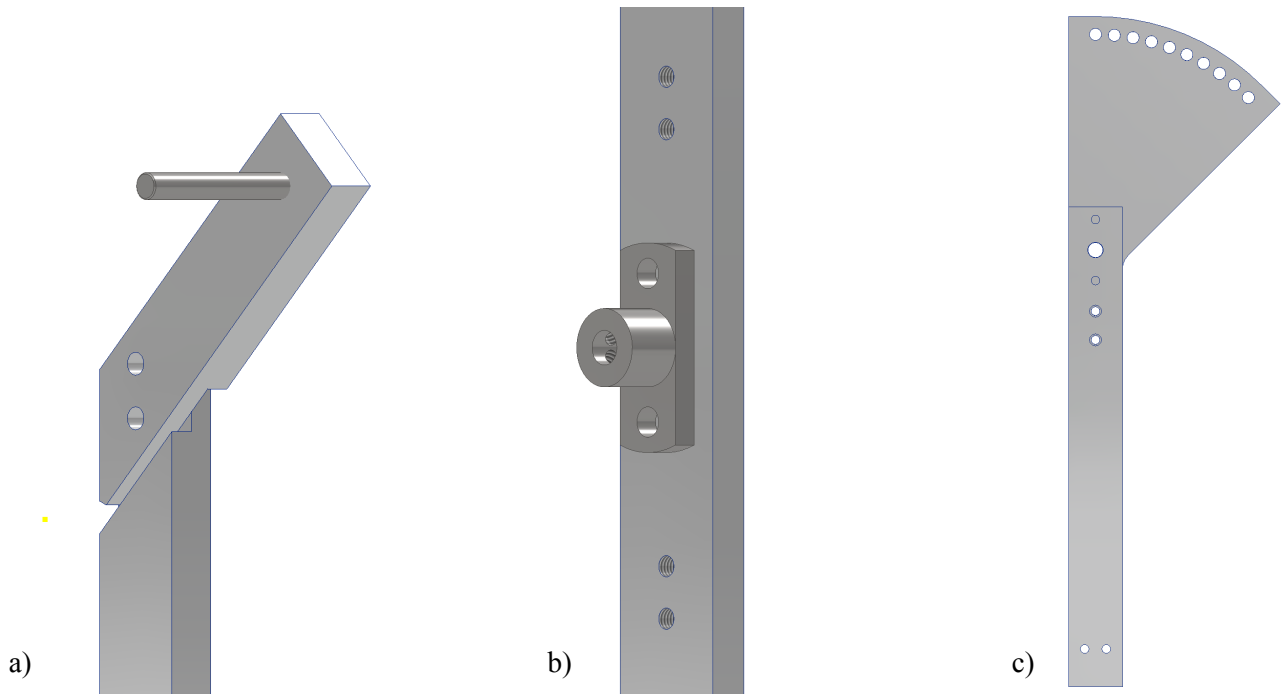


Figure 2.9: Shaft attached to back support (a), shaft collar to support rotation (b), and angle controlling fixture attached to the front support (c).

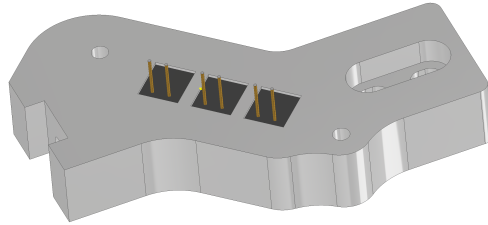


Figure 2.10: Halo MPPC fixture with MPPCs inside.

2.4.3 MPPC Fixture

In order to control the connection of the MPPCs and the fibers, a fixture was designed and 3D printed from acrylic. Due to the different number of channels in the halo and core regions, as described in Section 2.4.4, a separate design was done for each. An overhead view of the halo version of the fixture is shown in Fig. 2.10. This fixes the location of the MPPCs, shown in black, and contains screw holes on either side of the MPPCs to allow for attaching of the front-end board. Grooves can be seen on the left and right sides for attaching to the inner frame. The 3D print allowed for high precision of detailed features that would not have been otherwise achievable with traditional machining processes, such as perfectly square inside corners. A previous study performed by members at Osaka University, Kotera Katsuhige and Shimizu Nobuhiro, showed that using plastic greatly reduced the noise in the electronics compared to aluminum. The 3D printing also allowed for a short lead time which was desirable since the MPPC

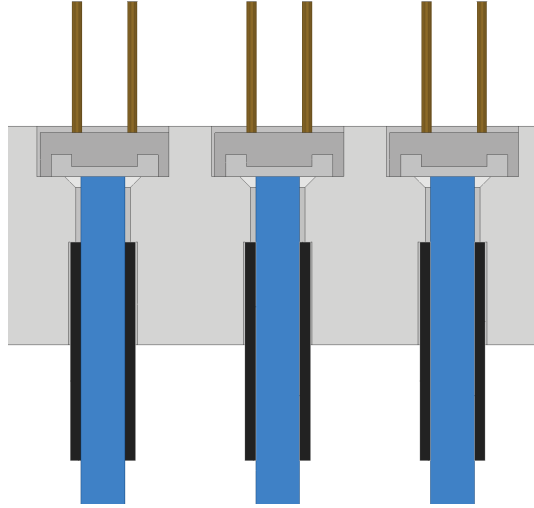


Figure 2.11: Cross section of MPPC fixture. The fibers (blue) are held in place by the carbon fiber collar (black) and are flush against the MPPCs (dark grey).

fixture was one of the last parts to be designed.

The MPPC fixture contained a 2.3-mm-deep recess for each MPPC to reside, allowing them to sit just below the back surface of the MPPC fixture as shown in Fig. 2.11. This allows a flush attachment of the front-end circuit boards. At the bottom of each recess are through holes for the fiber bundles to be inserted. The clearance in both the x and the y directions for the recesses was chosen to be 0.15 mm and the clearance for the through hole was chosen to be 0.5 mm. This is large enough to allow for fluctuations in the size of the MPPC and bundle as well as small enough to allow for the fiber ends to always be aligned with the photosensitive region of the MPPCs.

Due to the dispersion of light after leaving the fiber, the distance between the MPPCs and the fibers had to be controlled. From a study by a member at Osaka University, Hanai Kota, a 0.5 mm gap between the fibers and the MPPC would result in an 5% of the light being lost. The acceptable tolerance was chosen to be .5 mm. To control the insertion depth of the fiber bundles to the through holes, a carbon fiber sleeve was fixed around each bundle and the bundle's end was polished down to fit the required depth. The sleeve resided in its own recess on the side opposite to the MPPCs. Figure 2.11 shows the fibers inserted into the MPPC fixture with the carbon fiber sleeve controlling the distance of the fibers.

2.4.4 Core and Halo Separation

The front-end boards need to contain a circuit for each MPPC and therefore becomes significantly wider than the MPPC fixture as can be see in the left part of Fig. 2.12. If 24 modules were arranged in a planar shape the front-end boards would collide with the chamber wall in the z direction. By offsetting the top three modules (upper halo) and bottom three modules (lower halo) by 45° from the center eighteen modules (core) and reading them out from the opposite side, the UCV can provide complete coverage at any angle between 0° and 45° while not interfering with the chamber. This situation is shown in Fig. 2.13;

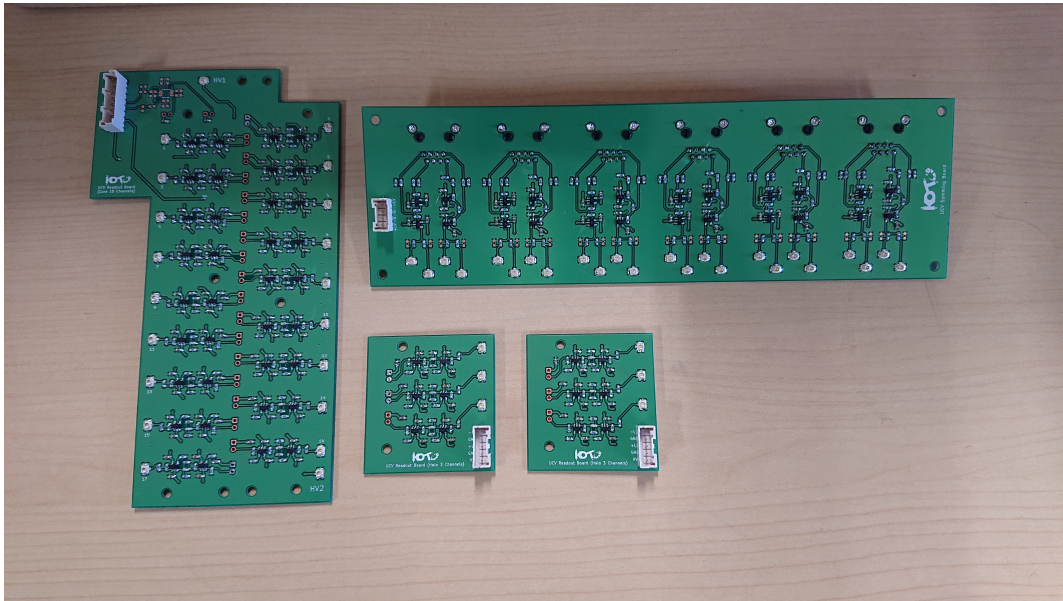


Figure 2.12: Front-end core board (right), front-end halo boards (top left), buffer board (bottom left).

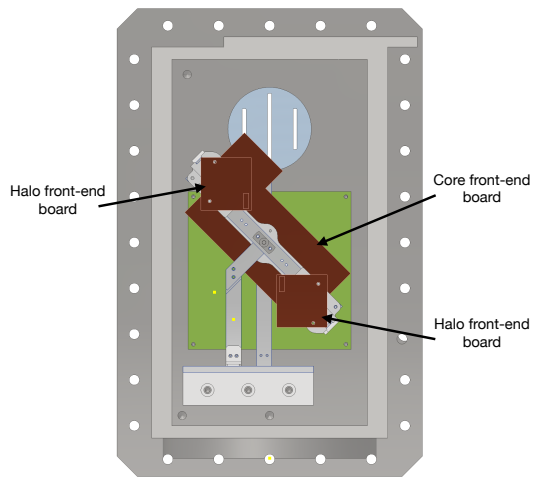


Figure 2.13: View of chamber with UCV tilted at 45° from the $-x$ direction. Circuit boards (red) do not interfere with the chamber walls.

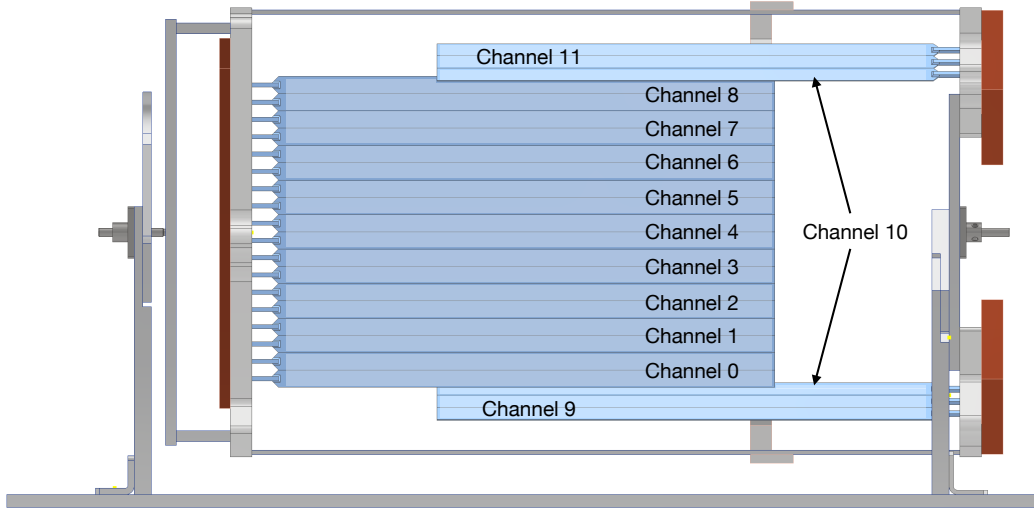


Figure 2.14: Channel assignment of the UCV.

the circuit boards do not collide with the chamber at 45° . The region between the core and the halo regions was designed with 3 mm of overlap. With low expected statistics in the halo region, the gap inefficiency in the halo modules was not considered an issue and the angle would be chosen based on the core region.

2.5 Electronics

2.5.1 Signal Readout

The front end circuit boards onto which the MPPCs are directly soldered were designed and developed by Ryota Shiraishi [12]. These boards amplify the signal and shorten the waveform. The signals from these boards are sent through a vacuum feed-through on the flange and into a buffer board. The buffer board sums two modules into one to reduce the number of channels from 24 to 12. The buffer board also creates a differential signal for the ADC. The ADCs record a 256-data-point (512 ns) waveform for each channel. Channel 0 through 8 are assigned to the core region while 9 through 11 are assigned to the halo region as shown in Fig. 2.14. Channel 10 is split between the top and bottom halo regions.

2.5.2 LED

In order to test the signal of each channel, an LED system was designed by a member at Osaka University, Kato Taishi, and was installed underneath the center of the UCV on the base-plate. The LED emits photons of 470 nm which is of similar wavelength to the scintillation light produced. The LED input signal is connected to an input driver that synchronizes all LED signals in the KOTO detector. One of the main functionalities of the LED is to measure the ADC count for a single photoelectron. Single photoelectrons generated by noise are not discernible because of their random timing and their similarity in height to Gaussian electronic noise. The LED provides pulses at a fixed time for easy separation

between single photoelectrons and noise. It can also be tuned to emit different amounts of light.

2.6 Replacement of MPPCs

The assembly of the UCV was designed in such a way that the MPPCs and the front-end boards could be replaced. This is crucial due to radiation damage. The MPPCs are soldered to the front-end boards so unscrewing the front-end boards from the MPPC fixture allows both to be easily removed. New MPPCs and front-end boards can be placed in the MPPC fixture, soldered together, and screwed in place.

Chapter 3

Performance Test

3.1 Purpose

To test the functionality of the UCV before installation at J-PARC, a beam test was done using a 584-MeV/c-momentum electron beam at The Research Center for Electron Photon Science (ELPH) at Tohoku University. The electron beam, providing a high purity source of charged particles, allowed us test the response of the electronics as well as measure the inefficiency of the UCV. Measuring the inefficiency was crucial to determine the angle before installation at J-PARC.

3.2 Experimental Setup

As at J-PARC, the lab coordinate system was defined as a right handed coordinate system with $+z$ pointing downstream of beam and $+y$ pointing vertically up.

The UCV was fixed to an aluminum extrusion frame sitting on top of a moving stage in the x -direction. The moving stage was able to be operated from the control room allowing for movement in the x -direction without stopping beam. Compared to the installation at J-PARC, the UCV was rotated 90° about the z axis so the positive x -axis of the UCV was inline with the positive y -axis of the lab frame. This was done to allow for more precision movement control across each channel. The moving stage was fixed atop of two lab jacks to allow for change in the y -direction.

As shown in Fig. 3.1, the UCV sat between a $60\text{ mm} \times 50\text{ mm}$ upstream and a $60\text{ mm} \times 40\text{ mm}$ downstream counter. Two additional tagging counters were placed just upstream and downstream of the UCV in order to more finely distinguish electron positions. The prototype UCV was placed upstream of and in a perpendicular orientation to that of the UCV allowing for measurement of the beam profile. All detectors and counters were wrapped in black vinyl to prevent contamination of ambient light. All detectors and counters were operated at atmospheric pressure.

The output signals from the UCV were connected to the same ADCs as they would be in J-PARC. The output signals for the counters were recorded in ADCs as well as sent to a trigger system. .

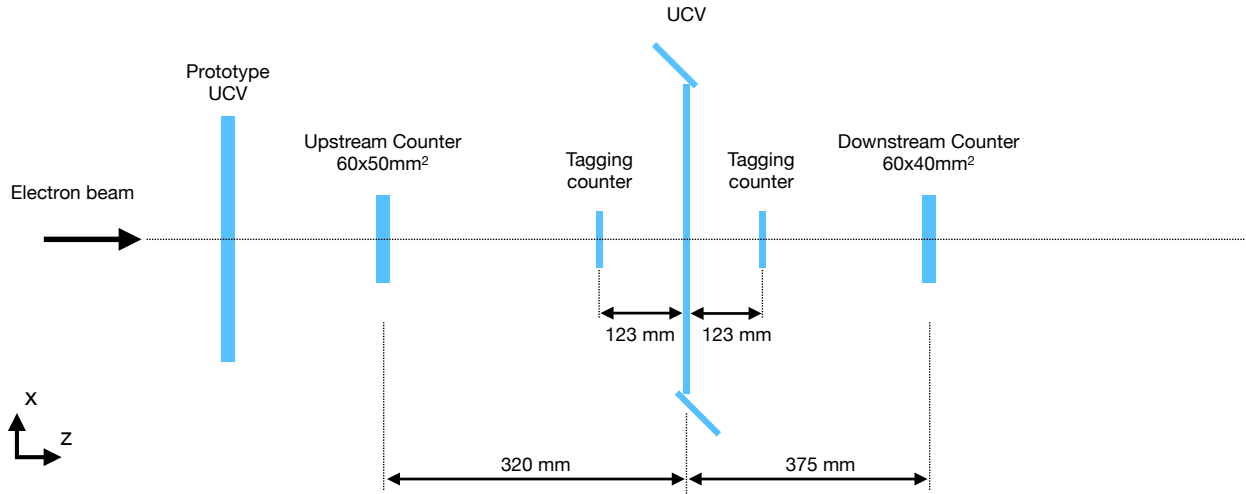


Figure 3.1: Setup of UCV and counters at ELPH.

3.3 Peak Detection method

The method to determine the energy deposited in the fiber is by measuring the heights of peaks in the waveform. Unless otherwise stated, all peaks in this paper were detected with the following method.

Peaks are calculated from the waveform. The timing range inside which the peaks were calculated is referred to as the peak detection window. Each sample inside the peak detection window, t , must satisfy the following conditions to be considered a peak:

$$f(t) \geq f(t + 1) \quad (3.1)$$

$$f(t) > f(t - 1) \quad (3.2)$$

$$f(t - 1) > f(t - 2) \quad (3.3)$$

$$f(t + 1) > f(t + 2) \quad (3.4)$$

$$f(t) > \text{peak threshold} \quad (3.5)$$

where peak threshold is a specific value which depends on the analysis. The timing of the peak is taken as t . Figure 3.2 shows an example of a peak being located.

Due to the nature of ADCs, the waveform baseline is not at zero ADC count. For each waveform the value of the baseline, called the pedestal, is calculated by comparing the average of the first 10 samples with the average of the last 10 samples and selecting the one with the smallest variance. For each peak the pedestal is subtracted to yield a value relative to zero.

3.4 Light Yield

To understand the light yield of the UCV, a run was taken without beam and with the LED tuned to emit single photons on average. Since the LED produces a consistently timed pulse, the peak detection

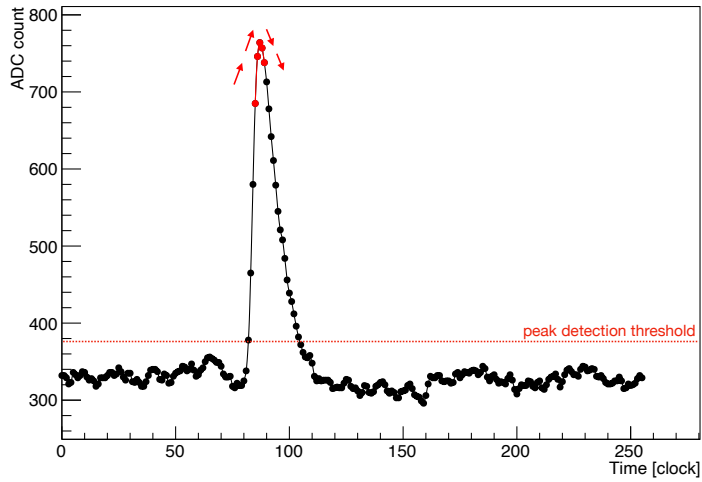


Figure 3.2: Peak being selected at ELPH data, where the red represents the structure that is searched for.

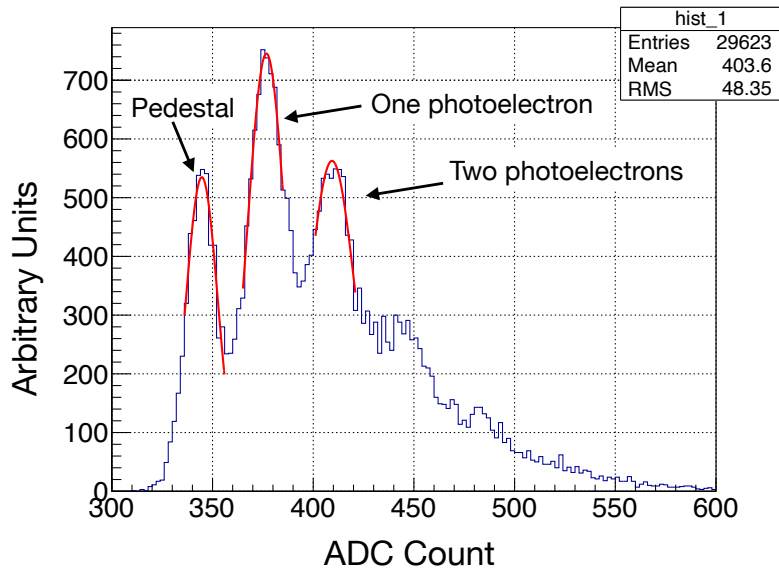


Figure 3.3: Distribution of measured peaks in channel 1 after the LED was set to emit single photoelectrons.

Channel	Single P.E. ADC	MIP ADC	Photoelectrons per MIP
0	29.77 ± 0.46	335.66 ± 2.38	11.28 ± 0.19
1	32.56 ± 0.41	382.65 ± 3.26	11.75 ± 0.18
2	34.22 ± 0.46	379.46 ± 3.37	11.09 ± 0.18
3	28.42 ± 0.36	412.21 ± 3.87	14.50 ± 0.23
4	30.06 ± 0.42	391.27 ± 2.19	13.02 ± 0.20
5	31.50 ± 0.42	394.74 ± 2.31	12.53 ± 0.18
6	28.84 ± 0.40	340.04 ± 2.47	11.79 ± 0.18
7	34.26 ± 0.50	385.99 ± 3.61	11.27 ± 0.20
8	34.27 ± 0.67	403.63 ± 4.29	11.78 ± 0.26
9	30.15 ± 0.74	362.46 ± 3.18	12.02 ± 0.31
10	30.46 ± 0.77	382.27 ± 2.97	12.55 ± 0.33
11	33.81 ± 0.44	353.9 ± 3.27	10.47 ± 0.17

Table 3.1: Distribution of single photoelectron ADC count and MIP ADC count per channel.

window was chosen to be 15 clocks centered on the nominal time. Since we wanted to measure low peak values, the peak detection threshold was set to zero. The resulting waveform peaks were plotted in a 1D histogram with clearly visible peaks corresponding to the pedestal, one photon, and two photons, as seen in Fig. 3.3. Each histogram peak was fitted to a Gaussian distribution and the distance between the one photoelectron peak and the two photoelectron peak was used as the ADC count corresponding to a single photon. The error was calculated by adding the fit error of each peak in quadrature. This was done independently for each channel.

Using the electron beam, the ADC value corresponding to a minimum ionizing particle (MIP) was calculated for each channel. Using the ADC count per single photon and the ADC count per MIP, the average number of detected photoelectrons per MIP was calculated for each channel. The results are shown in Table 3.1.

3.5 Inefficiency Measurement

3.5.1 Overview of Inefficiency

Particles are detected by the amount of energy they deposit. Some particles deposit a small amount of energy and are therefore indistinguishable from noise. To minimize the accidental loss, a threshold is set on the deposited energy. Only peaks that cross that threshold are considered hits, therefore inefficiency is defined as the fraction of particles whose energy deposition falls below the threshold.

To measure the inefficiency, we first select a sample of events that are a pure source of charged particles passing perpendicular to the plane of the UCV. Our data sample consists of events triggered on coincidence between the upstream and downstream counters. For each event, peaks are calculated in a 10 clock peak detection window centered on the nominal time with no peak detection threshold. The peaks are then normalized to units of MIP. The deposited energy for any given event was chosen to be the largest peak out of all the channels.

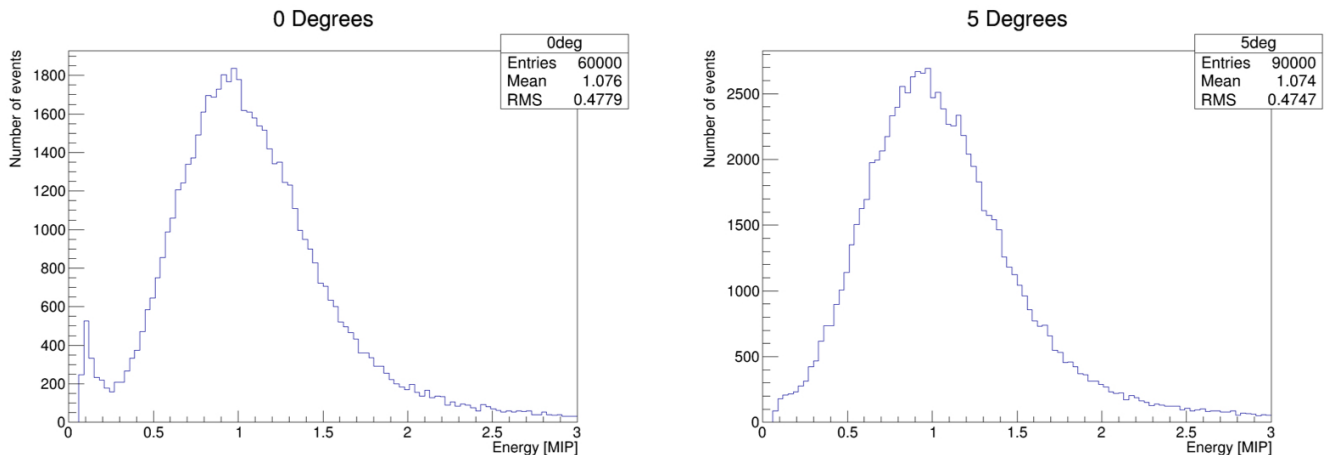


Figure 3.4: Deposited energy distribution with UCV at 0° (a) and 5° (b).

3.5.2 Sources of Inefficiency

The energy deposition of a charged particle in scintillation material follows a Landau distribution. Due to the discrete nature of photons produced in the scintillation material and detected at the MPPCs, the Landau distribution is smeared by a Poisson distribution centered on the average number of detected photons. This smearing effect becomes larger as the average number of detected photons becomes smaller, resulting in a wider energy distribution. In turn, the energy of some events fall below the threshold causing inefficiency.

Additional smearing in the energy distribution comes from the imperfections in the signal readout. The front-end electronics produce Gaussian noise. This noise mixes with the signal and causes variations in the calculated peak, hence widening the energy distribution.

As explained in Section 2.4.2, events that pass through gaps between fibers deposit no energy and therefore the measured peak lies at the pedestal.

3.5.3 Angle Scan

The UCV was tested at different angles ranging from 0° to 45° at 5° increments with the beam centered in the UCV. At 0°, the deposited energy distribution has a clear peak at the pedestal as shown in Fig. 3.4a. The number of events below 0.25 MIP at 0° corresponds to $(3.98 \pm 0.08)\%$ of the total. This is consistent with the thickness of the cladding (4% of the UCV). The peak decreases in height as the angle increases which can be seen in Fig. 3.4b. Inefficiency calculations for low angle as a function of threshold are shown in Fig. 3.5. All angles below 0.5 MIP satisfy our inefficiency requirement of 10%.

When considering a low threshold as in Fig. 3.6a, a small increase in the angle results in a large reduction in inefficiency. This is because the contribution from particles that passed through the gap now have energy above the threshold. When looking at higher thresholds however as in Fig. 3.6b and Fig. 3.6c, the increase in angle has less of an effect because a smaller portion crosses the threshold.

When the angle is tilted past 2.3° but less than 45°, all particles that pass through the UCV will come into contact with scintillation material. As shown in Fig. 3.7 in this situation the particle passage can

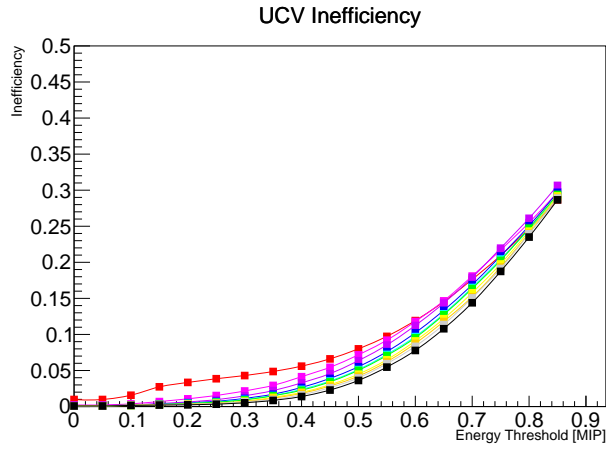


Figure 3.5: Inefficiency of UCV tilted at 0°(red), 5°(pink), 10°(purple), 15°(blue), 20°(cyan), 25°(green), 30°(yellow), 35°(orange), 40°(grey), and 45°(black) as a function of energy threshold.

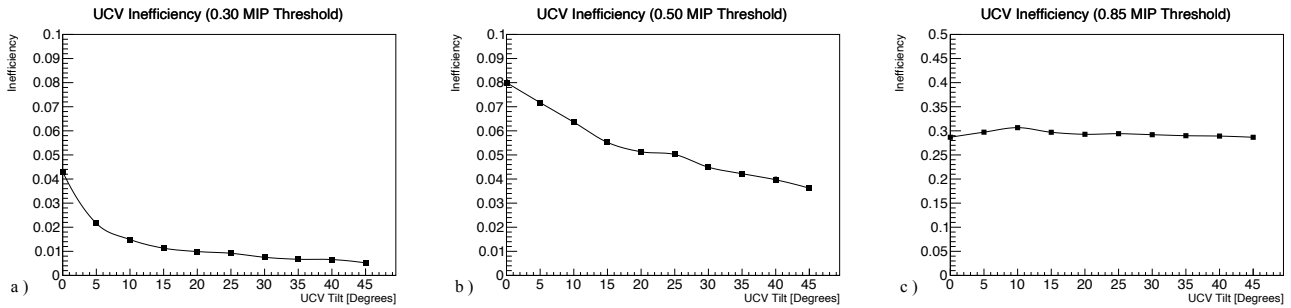


Figure 3.6: Change in inefficiency with angle at 0.3MIP threshold (a), 0.5MIP threshold (b), and 0.85 MIP threshold (c).

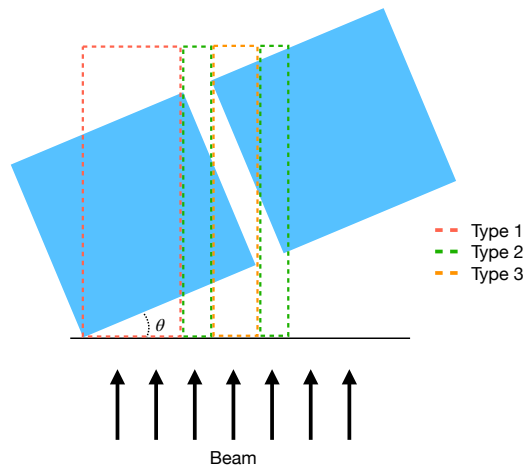


Figure 3.7: Three types of particle passage through the UCV when tilted past 2.3°.

be categorized as three types, complete passage through one fiber (type 1), passage through one fiber and the gap (type 2), and passage through two fibers and the gap (type 3). For square fibers the length of interaction with scintillation material, for particles that have no x direction or y direction momentum, follows the relations

$$x = \frac{t}{\cos \theta} \quad (3.6)$$

$$x = \frac{t}{\cos \theta} - \frac{ga}{\sin \theta} \quad (3.7)$$

$$x = \frac{t}{\cos \theta} - \frac{g}{\sin \theta}, \quad (3.8)$$

for type 1, 2, and 3 respectively, where t is the thickness of the scintillation material, g is the width of the gap, θ is the tilted angle and a varies between 0 and 1 linearly, depending on the particle position. The probability of occurrence for each type of event follows the relations

$$p(\text{type1}) = \frac{t}{t+g}(1 - \tan \theta) \quad (3.9)$$

$$p(\text{type2}) = \frac{2g}{t+g} \quad (3.10)$$

$$p(\text{type3}) = \frac{t}{t+g} \tan \theta - \frac{g}{t+g}. \quad (3.11)$$

Multiplying the length of interaction by the probability of occurrence and summing each type gives the average length of interaction for the UCV as

$$x = \frac{t^2}{(t+g) \cos \theta}.$$

From equations (3.9) and (3.11) we can see that the percentage of type 1 events will decrease while the that of type 3 events increase with increasing angle; however, if the light yield of type 3 events is lower than the threshold those events will contribute to inefficiency. Looking at 10° for example, the length of interaction for type 3 is only 0.37 mm meaning the average light yield for these events will be decreased to 77%. At 10° type 3 consists of 13 % of the total events. This has a larger effect at higher thresholds, and at 0.85 MIP threshold we can see the inefficiency increase at 10° as shown in Fig. 3.6c. As will be discussed in Section 4.6 the threshold will be set low enough that increasing the angle will decrease the inefficiency.

3.5.4 Position Scan

To confirm the overall inefficiency of the UCV was consistent at different locations, inefficiency measurements were taken at different x and y positions at 25° . The x and y positions were chosen so that every point in the core region was covered within 1σ of the beam width. All locations resulted in an inefficiency less than 1% different than that of the center as shown in Fig. 3.8.

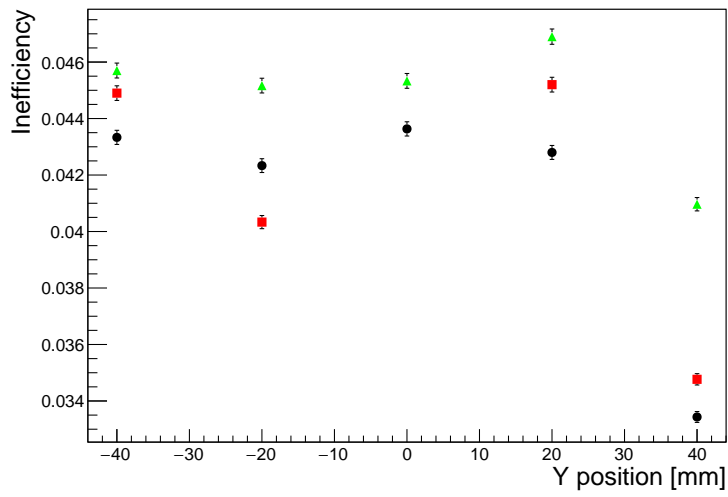


Figure 3.8: The inefficiency at different y positions of the UCV at x positions of -43 mm (black), 0 mm (red), and 43 mm (green).

Chapter 4

Estimation of Accidental Loss

4.1 Overview of Accidental Loss

4.1.1 Definition of accidental loss

The key characteristic of $K_L \rightarrow \pi^0 \nu \bar{\nu}$ is a lack of signals in veto detectors. When we have a true $K_L \rightarrow \pi^0 \nu \bar{\nu}$ event, we may have hits in veto detectors due to noise or accidental particles. This results in vetoing $K_L \rightarrow \pi^0 \nu \bar{\nu}$ events and lowers our acceptance. The ratio of $K_L \rightarrow \pi^0 \nu \bar{\nu}$ events that we veto to all $K_L \rightarrow \pi^0 \nu \bar{\nu}$ events is referred to as accidental loss.

This study was focused on two main sources of accidental loss produced by the UCV, noise from the electronics and hits from beam particles. Noise from electronics comes from the inherent Gaussian noise and dark current from the MPPCs. Due to prolonged exposure to neutron radiation, the MPPCs dark current will slowly increase over time. Accidental loss from beam particles comes from hits in the UCV by particles other than decayed event of interest. Since both effects are uncorrelated to the $K_L \rightarrow \pi^0 \nu \bar{\nu}$ event, we want to evaluate them with a set of randomly triggered data.

4.1.2 Target for UCV

Most detectors in the KOTO experiment individually have $\mathcal{O}(1-10)\%$ accidental loss. To obtain a similar level of quality to other detectors and to not significantly increase the total, the goal for the UCV was set to $\mathcal{O}(5\%)$ accidental loss.

4.2 Method to Simulate Data

4.2.1 Selection of method

In order to estimate the accidental loss, randomly triggered data needs to be simulated. For this study two different methods were chosen.

For one method the effect of dark current was evaluated by overlaying photoelectron pulses on a base waveform and performing the same analysis that would be done with real data. The effect from beam particles was evaluated using the KOTO beamline simulation and a Monte Carlo software package called

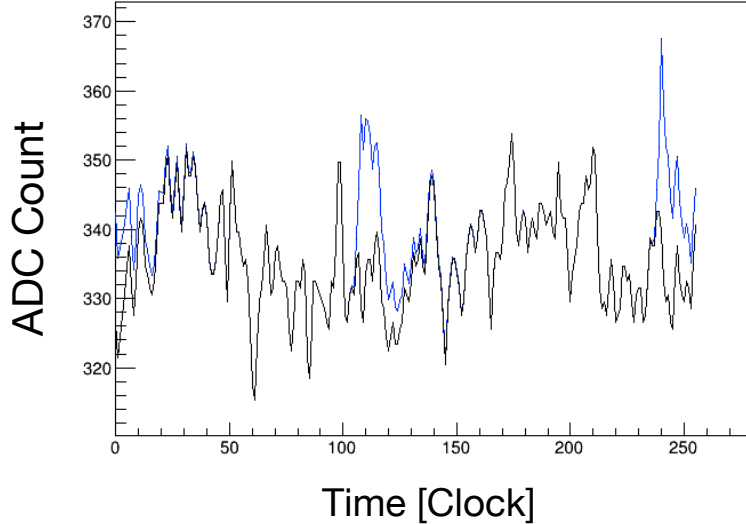


Figure 4.1: Overlay of waveforms during the generation process for base waveform (black) and after photoelectron overlay (blue).

Geant4. Both effects were normalized by their respective rates and the total accidental loss was taken as the sum of the two effects.

For the second method the effect of dark current and beam particles were evaluated by overlaying photoelectron pulses from both effects on a base waveform and performing the same analysis that would be done with real data, where the base waveform contains only the inherent Gaussian noise. This creates a data set similar to that which we collect at J-PARC for accidental loss analysis.

For the selection of the angle before installation of the UCV the former method was used, but after installation the method was changed to the latter. Both methods yield similar results and the decision on the angle would not have differed between either method. The latter method was used for the majority of the analysis following installation and is therefore the method described in this thesis.

4.2.2 Waveform simulation

Base waveform data is collected with the MPPCs unpowered and without beam. This contains only the noise from electronics and the environment. Single photoelectron pulses from dark current are overlaid on the base waveform. Pulses due to energy deposition from beam particles are further overlaid on top.

The pulse template that is used for the overlay is a piece-wise function of exponentials,

$$\begin{cases} Ae^{-\frac{x}{3.6}} & x \leq 0 \\ Ae^{-\frac{x}{18}} & x > 0 \end{cases}$$

where x is measured in nanoseconds and A is normalized to the energy of the pulse as shown in Fig. 4.2. The decay time constant was obtained from fitting real waveform pulses to data. The rise time constant was set 5 times smaller due to the steep rising edge of the real waveform. An example of waveforms before and after photoelectron overlay can be seen in Fig. 4.1 where black is the waveform before overlay and

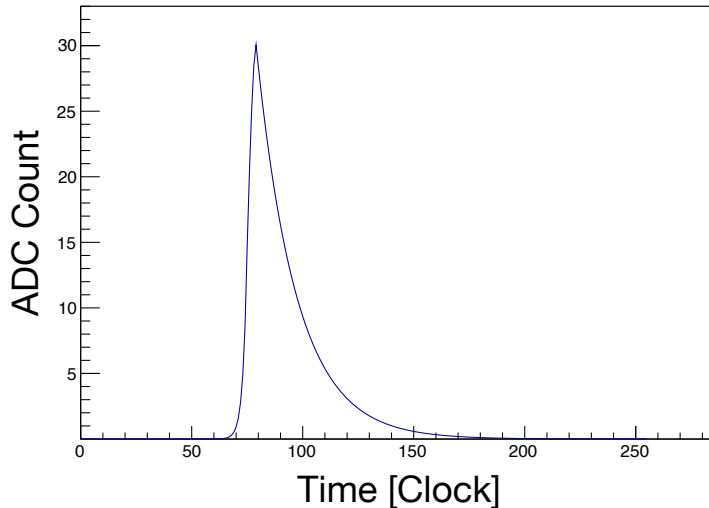


Figure 4.2: Pulse generated at single photoelectron level before overlay located at a random time.

blue is the waveform after overlay.

For each event the number of overlaid pulses was randomly chosen from a Poisson distribution centered on the average. The average number of pulses is taken to be the rate of occurrence multiplied by the waveform width. See Sections 4.3.1 and 4.4.3 for rate calculations.

Real pulses are randomly distributed in time, some of which occur at the beginning or the end of the waveform with the head or tail cut off. To account for this, each simulated pulse is overlaid at random time intervals inside a 768 clock waveform. The center 256 clock is selected and summed onto the base waveform.

For real data if the energy deposition is too high, the electronics will saturate and the peak in the waveform will be cut off. The saturation value corresponds to between 2000 and 3000 ADC count, differing between channels. To account for this the overlaid waveforms were cutoff at the respective ADC counts for each channel.

4.2.3 MPPC Crosstalk

The height of each overlaid pulse was normalized to a discrete number of photoelectrons. For each photoelectron in each pulse, a random value between 0 and 1 was selected. If this value was smaller than the crosstalk probability, an additional photoelectron was added for that pulse. For the newly added photoelectron, the same process was applied.

The crosstalk probability was calculated from beam-off clock-triggered data. The major source of measured energy in beam-off events comes from dark current. Since the rate of two pixels generating a photoelectron at the same time is small, all instances of greater than one photoelectron are assumed to have resulted from crosstalk. The peak distribution of beam-off data was compared to that of simulated data with different levels of crosstalk. Figure 4.3 shows the comparison of energy deposition between simulated waveforms and beam-off data. In the left side the simulation uses a crosstalk probability 7% while the right side uses 15%. The crosstalk probability was chosen to be 15% for simulation.

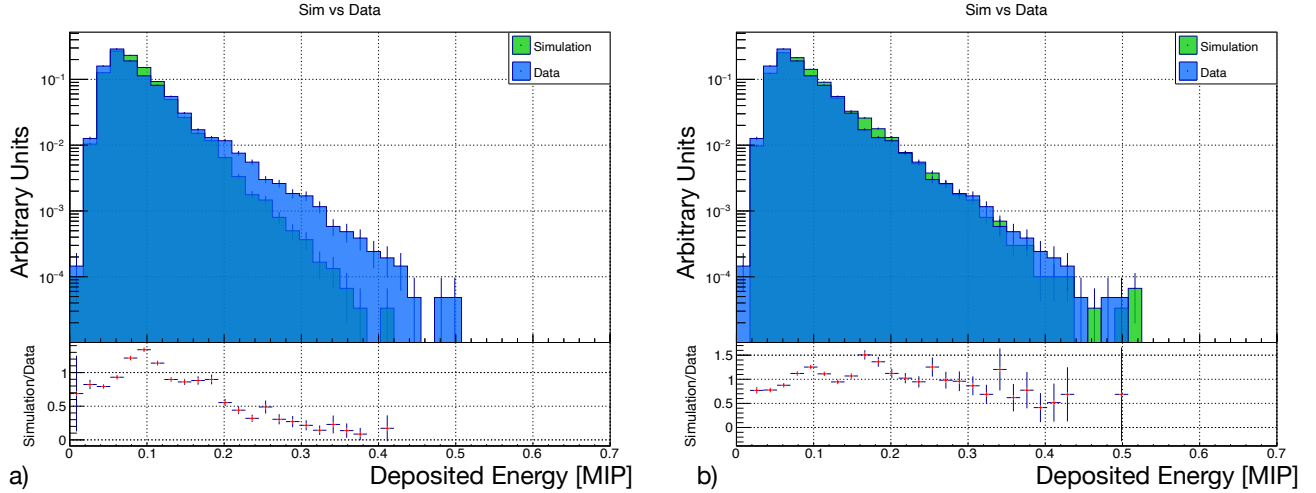


Figure 4.3: Peak distributions comparing data with simulation at a simulated crosstalk level of 7% (left) and 15% (right).

4.3 Dark Current

4.3.1 Rate Calculation

The rate of single photoelectron generation can be calculated from the amount of current that the MPPC produces. Attached to the UCV is an MPPC whose purpose is to measure the dark current with change in irradiation. The MPPC is covered to prevent light from entering.

Knowing the gain of the MPPC and the charge of a single electron we can calculate the rate of electrons from the MPPC. Due to the effect of crosstalk, not all generated pulses will have a height of one photoelectron and the rate needs to be modified accordingly. The rate is calculated by,

$$Rate = \frac{Current}{Gain \times e \times N_{Crosstalk}},$$

where the gain is taken from the catalog value and $N_{Crosstalk}$ is

$$N_{Crosstalk} = \frac{1}{1 - r}$$

where r is the crosstalk probability.

4.3.2 Irradiation Effect

Due to the large number of neutrons in the beam and their proximity to the UCV, the UCV suffers from non-negligible radiation damage to its MPPCs. The incident neutrons knock atoms out of the crystal lattice and create impurities. These impurities cause an increase in dark current. Before installation of the UCV at J-PARC, a study was conducted by a member at Osaka University to measure the effect of neutron damage on MPPCs. The study concluded the dark current increase at the UCV location to be $0.98 \mu A$ per day. With 20 days of beam time planned in spring 2021, the dark current was expected to

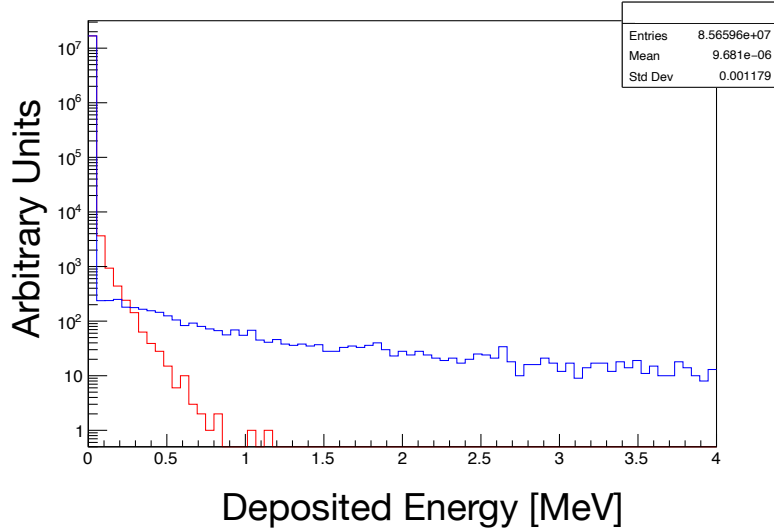


Figure 4.4: Geant4 simulation of neutron (blue) and photon (red) energy distribution in the UCV.

end at $19.6 \mu\text{A}$.

4.4 Beam Particles

4.4.1 Mechanism

The majority of the energy deposition in the UCV due to beam particles comes from neutrons and photons as seen in Fig. 4.4. Neutrons scatter off the nucleus of the material in the plastic resulting in ionization. Photons primarily deposit energy by pair production, where the resulting electron and positron interact with the scintillation material. The effect from beam particles remains constant in time but scales linearly with beam power (due to the fact that more particles are produced).

4.4.2 Geant4 Simulation

Geant4 was used to simulate the energy deposition of beam particles in the UCV. The input particles were generated using the output of the official KOTO beamline simulation. The detector geometry and material were constructed based on the real UCV. Simulations were done with the UCV rotated at each angle. The resulting energy distributions were used to produce waveforms.

4.4.3 Beam Normalization

The rate of beam particles is determined by the beam power. The number of protons incident on the target (PoT) per cycle can be calculated from the beam power as

$$\#\text{PoT per cycle} = \frac{(\text{cycle length}) \times (\text{beam power})}{30 \text{ GeV}}$$

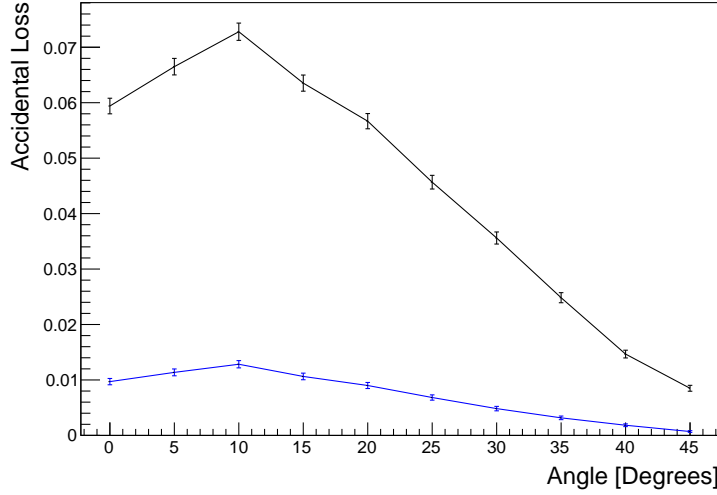


Figure 4.5: Simulated accidental loss vs angle with dark current of $2\mu\text{A}$ (blue) and $20\mu\text{A}$ (black).

where each cycle at J-PARC lasts 5.5 seconds. The KOTO beamline simulation corresponds to 10^{12} PoT and contains 17.4×10^6 entries. The incident rate in the UCV is given by

$$\text{Rate} = \frac{17.4 \times 10^6 \text{ entries}}{10^{12} \text{ PoT}} \times \# \frac{\text{PoT}}{\text{cycle}} \times \frac{1}{2.2 \frac{\text{s}}{\text{spill}}}$$

where $2.2 \frac{\text{s}}{\text{spill}}$ comes from the fact that all of the protons are delivered in the first 2.2 s of each cycle.

4.5 Expected Accidental Loss

4.5.1 Calculation of accidental loss

From the simulated data set the peaks are calculated as described in Section 3.3. For each event the largest peak inside a 20 ns window across all channels is selected. This is referred to as the veto peak. If the veto peak crosses the threshold, the event is considered to have a hit. The loss is calculated as follows:

$$\text{Loss} = \frac{\# \text{ events with hits}}{\# \text{ total events}}$$

4.5.2 Dark Current

The change in angle affects accidental loss from dark current only by means of changing the threshold. The threshold is held at a constant ratio of MIP energy deposition. Due to the effect of the gap, the MIP energy distribution has a peak at 10° . After further increase from 10° , the MIP energy deposition increases and therefore the threshold increases. In Fig. 4.5 can see this same structure in the accidental loss.

Since the effect from dark current comes from single photoelectrons, modified by crosstalk, it is expected that the peak distribution is centered at a very low value and decays exponentially with increasing

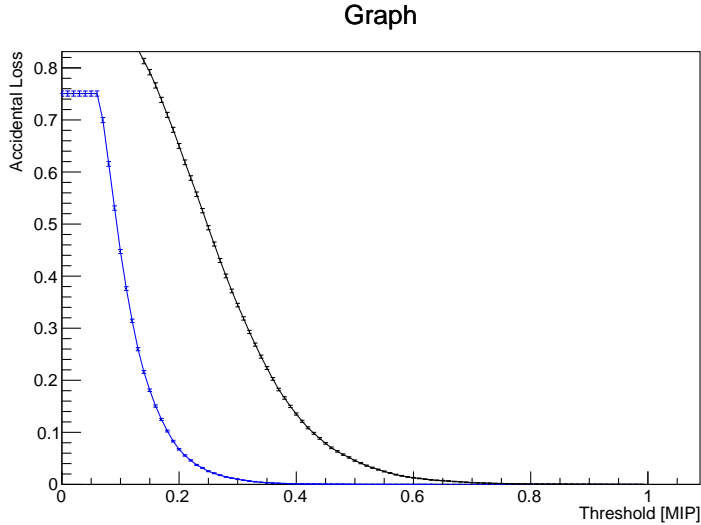


Figure 4.6: Accidental loss simulation without beam as a function of threshold at 0° tilt with dark current of $2\mu\text{A}$ (blue) and $20\mu\text{A}$ (black).

threshold. The accidental loss decreases with increasing threshold as seen in Fig. 4.6. At $20\ \mu\text{A}$ the accidental loss from the dark current alone results is 4% at 0.5 MIP threshold.

4.5.3 Beam particles

The beam particles are expected to cause an accidental loss that is independent of irradiation. Comparing Fig. 4.7 and Fig. 4.5 we can see an increase in the accidental loss of around 1%

4.6 Threshold and Angle Selection

The threshold needs to be set high to minimize the accidental loss and need to be set low to minimize the inefficiency. As explained in Section 3.5.3, to overcome a large portion of the inefficiency from the gap at thresholds below 0.5 MIP, the angle should be greater than or equal to 15° . From Fig. 4.7 the accidental loss at 15° is approximately 9%. Increasing the tilt to 25° reduces the accidental loss to 7%. Assuming a fixed threshold of 0.5 MIP, 7% inefficiency would be an acceptable accidental loss at the end of the spring 2021 where the average across the entire run would be less than 5%.

Furthermore, due to the uncertainty of the irradiation-increase estimate described in Section 4.3.2, there was a concern that the true irradiation would be larger and therefore the accidental loss from dark current would be greater. Setting the tilt to a higher angle would provide a factor of safety against irradiation. The angle was set to 25° based on these factors.

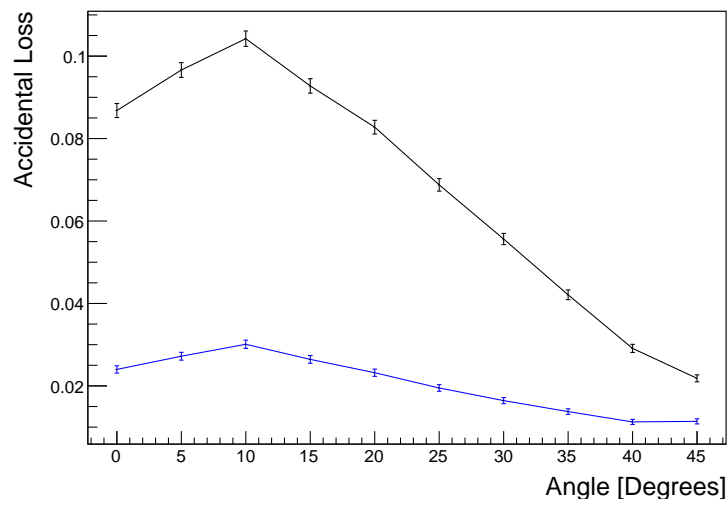


Figure 4.7: Simulated accidental loss vs angle for beam particles at 0.5 MIP threshold at 10 μA of dark current (blue) and 20 μA of dark current (black).

Chapter 5

Functionality at J-PARC

5.1 Installation

The UCV was installed in December 2020 for operation starting in the spring of 2021. After installation, data was taken to test the functionality without beam, including measurements of the single photoelectron ADC count and level of noise.

5.2 Beam Test Comparison

As can be seen in Fig. 5.1, the ADC counts corresponding to single photoelectrons were calculated at J-PARC and compared to the estimate at ELPH. The value at ELPH was between 5% and 25% higher than that at J-PARC for most channels. This may be due to the longer cable length used at J-PARC, causing attenuation of the signal.

To calibrate the energy of the detector at J-PARC, a run was taken with the beam plug closed. This produces a large number of muons and is referred to as a muon run. The value at ELPH is between 10% and 20% higher for most channels. Using the ADC count per MIP and the ADC count per single photoelectron, the number of photoelectrons per MIP, light yield, was calculated as shown in Fig. 5.2. The light yield between ELPH and J-PARC are within 10% of each other.

The base noise at J-PARC follows a Gaussian distribution with a standard distribution of (10.7 ± 0.005) ADC counts. This is slightly smaller than the ELPH value of (11.3 ± 0.005) ADC counts as shown in Fig. 5.3. The difference in single ADC count level and was not taken to be a significant effect.

5.3 Beam Coverage

Using a run at J-PARC with the sweeping magnet turned off, the hit distribution was calculated for each channel as shown in Fig. 5.4. For each event the maximum peak was selected for each channel. If the channel had at least one hit in the waveform, the histogram was filled once for that channel.

There is a large number of hits between channels two and seven. The rate drops significantly at channels one and eight, both of which are core channels. Most charged particles are well contained inside

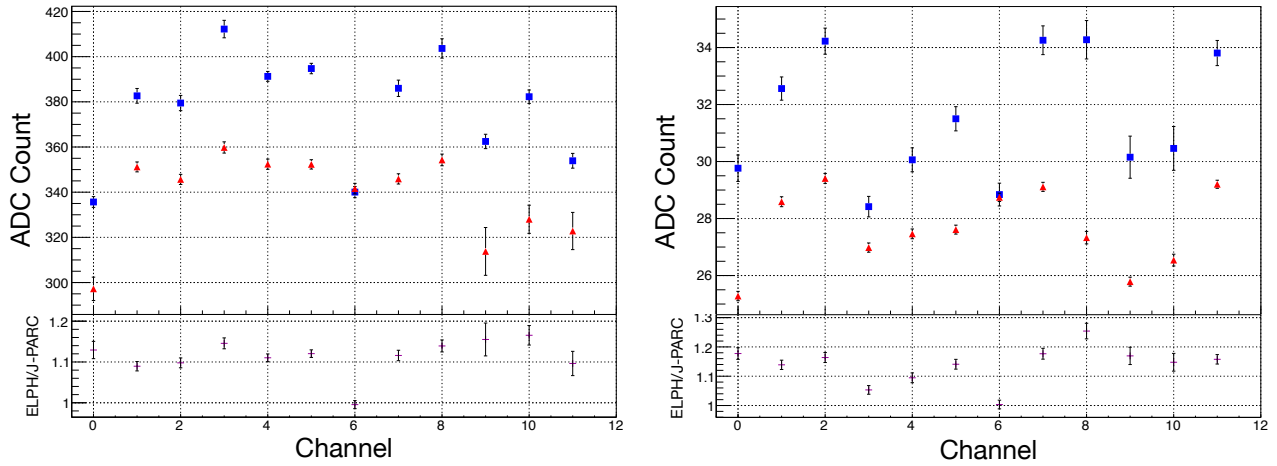


Figure 5.1: Comparison of ADC count for MIP peak calibration values (left) and single photoelectrons (right) between ELPH (blue) and J-PARC (red). The ratio of ELPH to J-PARC is shown in the bottom.

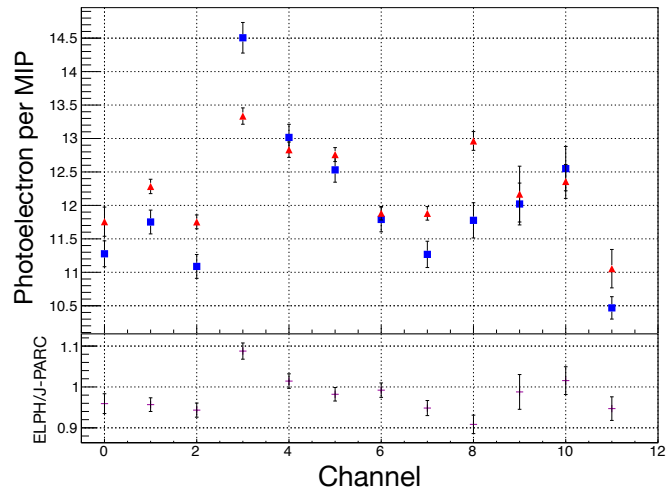


Figure 5.2: Comparison of ADC count for MIP peak calibration values (left) and single photoelectrons (right) between ELPH (blue) and J-PARC (red). The ratio of ELPH to J-PARC is shown in the bottom.

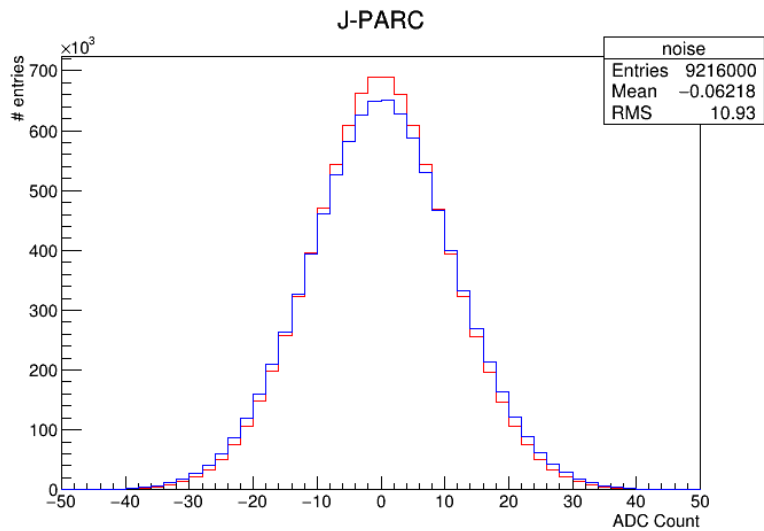


Figure 5.3: Distribution of waveform samples with MPPCs turned off at ELPH (blue) and J-PARC (red).

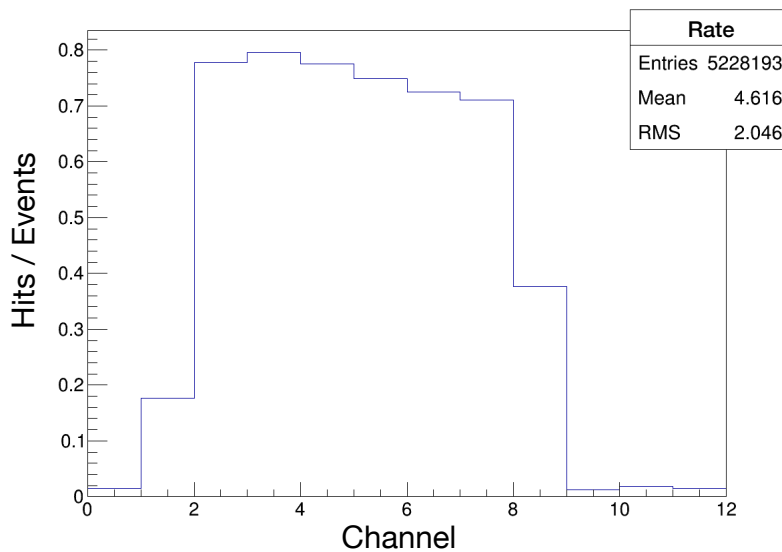


Figure 5.4: Hit distribution per channel with sweeping magnet turned off.

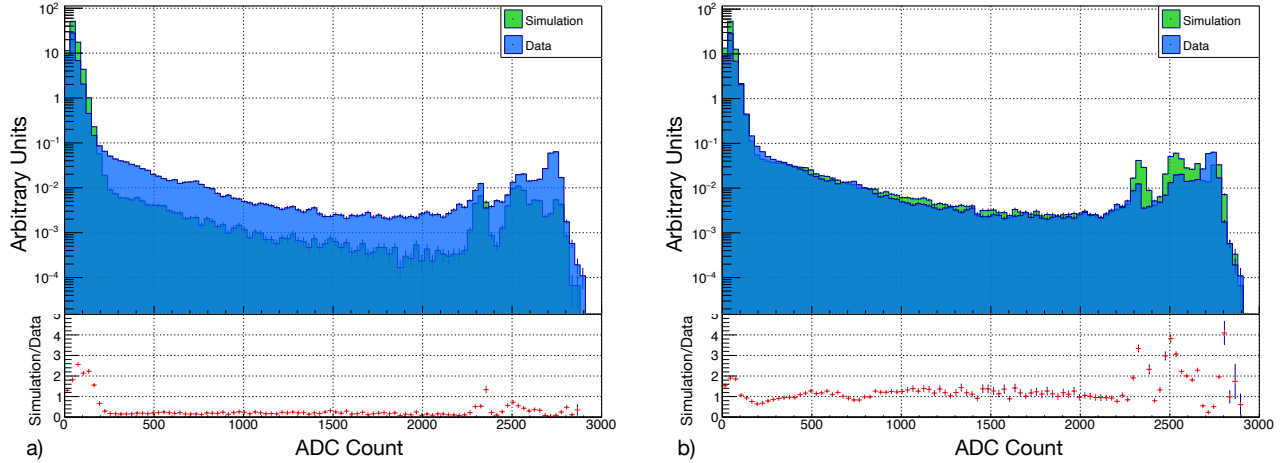


Figure 5.5: Comparison of energy deposition for TMon data and simulated data before normalization (a) and after normalization (b).

the core region of the UCV.

The geometric center of the UCV is located in the center of channel four, however, the beam flux is centered between channel 4 and channel 5. The difference between the geometric center of the UCV and the center of the beam flux is approximately 10 mm. This may result from imperfect beam alignment or deflection of the flange in the chamber. Extra support to prevent deflection was added in June 2021. Since the beam is located within the core region on the UCV, the positioning was considered acceptable and further modifications were not made.

5.4 Accidental Loss

5.4.1 Data Selection

To estimate the effect of accidental loss, a random trigger is needed to select data. Three scintillation counters are placed 50° off the axis of extraction downstream from the target and coincidence on them is taken as trigger. The trigger therefore depends on the beam power but not on the KOTO detector. Data collected with this trigger is referred to as Target Monitor (TMon) data. Fluctuations in the beam structure have an effect on the instantaneous trigger rate of physics data and TMon data, increasing trigger rate with beam intensity. This effect is not seen in clock data.

5.4.2 Calculation method

The accidental loss (at J-PARC) is calculated with TMon data. The calculation method is the same as described in Section 4.5.1.

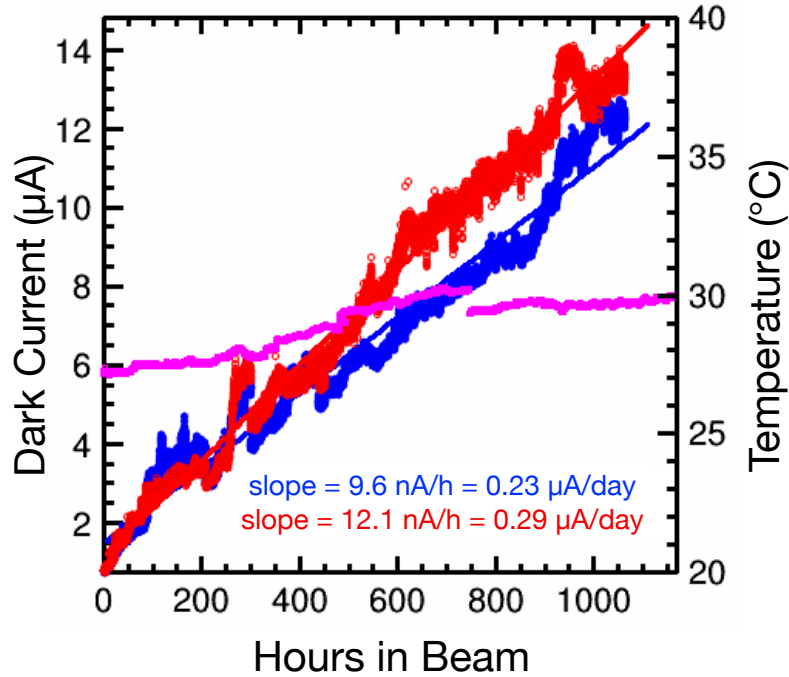


Figure 5.6: UCV monitor dark current as a function of beam time for two different dark current monitors.

5.4.3 Comparison to Simulation

The peak distribution of accidental hits was compared between simulation and data, as shown in Fig. 5.5. The left graph shows the distribution before any normalization. There is a factor of 6 discrepancy between data and simulation due to beam particles as can be seen in the center region of Fig. 5.5a. The rate of beam particles was normalized by a factor of 6 and the dark current was normalized by a factor of 0.5. The result is shown in the right graph.

Using the irradiation monitor we tracked the dark current as a function of time in beam as shown in Fig. 5.6. Fitting this graph linearly, the value of dark current measured at J-PARC is $0.29 \mu\text{A}$ per day, approximately $\frac{1}{3}$ that of the expectation.

5.5 Inefficiency

5.5.1 Charged Kaon Reconstruction

To measure the inefficiency at J-PARC we need a good sample of charged particles. Charged Kaons, which are the particles the UCV was designed to veto, provide a clean sample.

Specifically we look at charged kaons that decay by $K^\pm \rightarrow \pi^\pm \pi^0$. All three final particles are measured as energy clusters in CSI. The π^\pm additionally leaves a signal in CV. There are no signals in other detectors.

Events for charged kaons are triggered when there is an energy deposition in CSI and in CV.

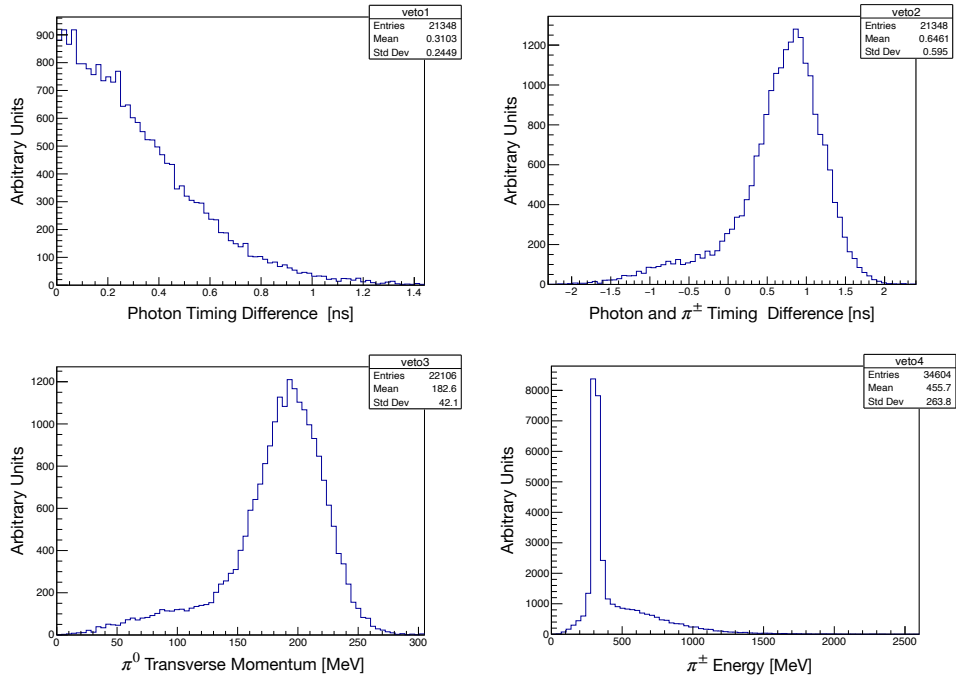


Figure 5.7: Distributions of photon timing difference (top left), photon and charged pion timing difference (top right), neutral pion momentum (bottom left), and measured charged pion energy (bottom right) with all cuts applied except the shown variable..

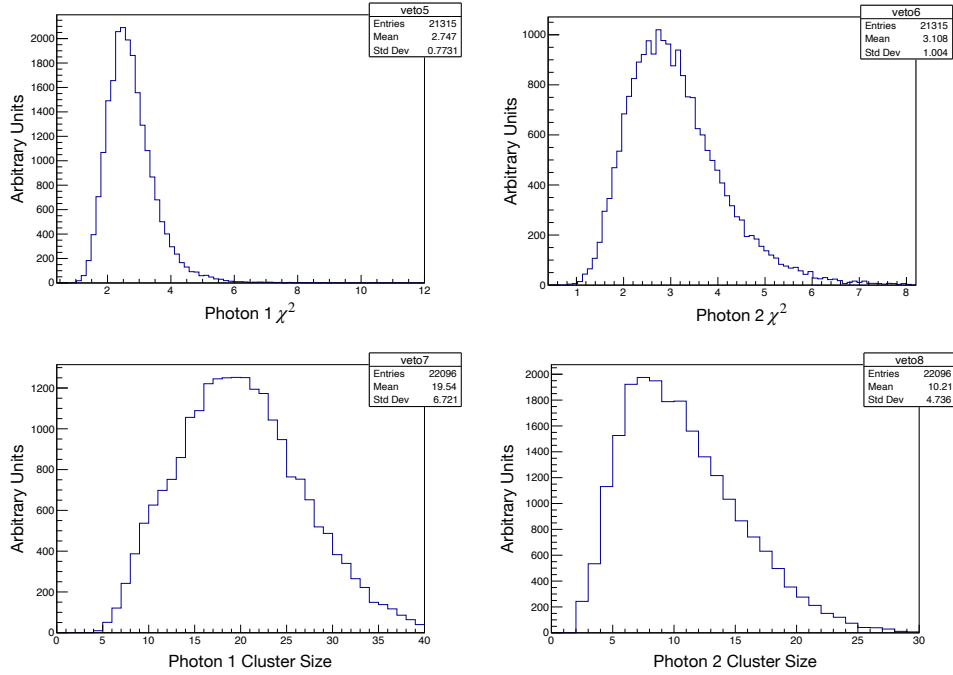


Figure 5.8: Distributions of photon χ^2 values (top) and photon cluster sizes (bottom) with all cuts applied except the shown variable.

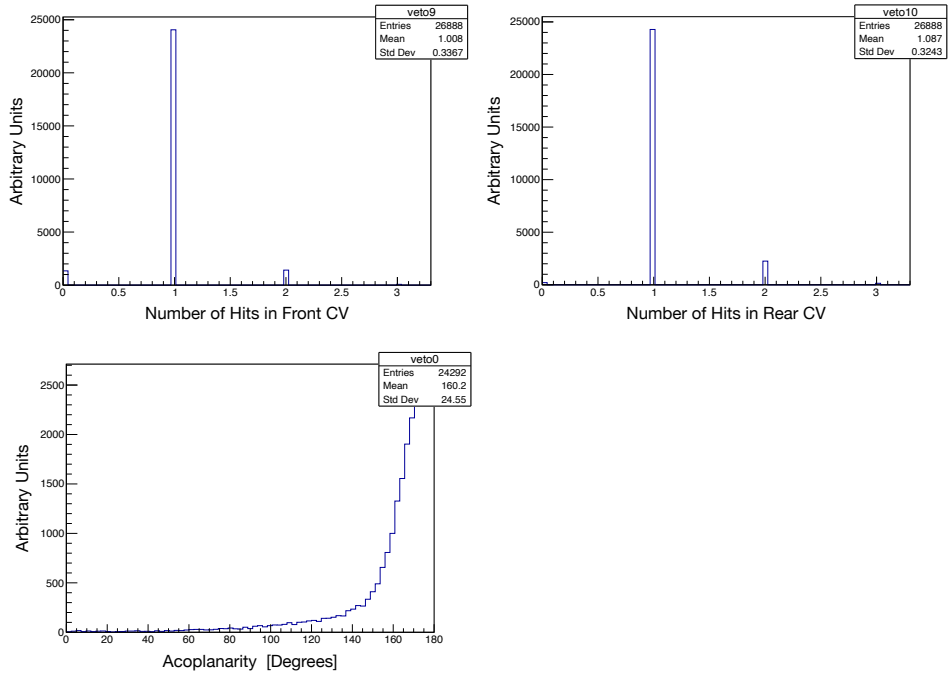


Figure 5.9: Distributions of number of hits in the front CV (top left), number of hits in the rear CV (top right), and angle between the π^0 and the π^\pm (bottom) with all cuts applied except the shown variable.

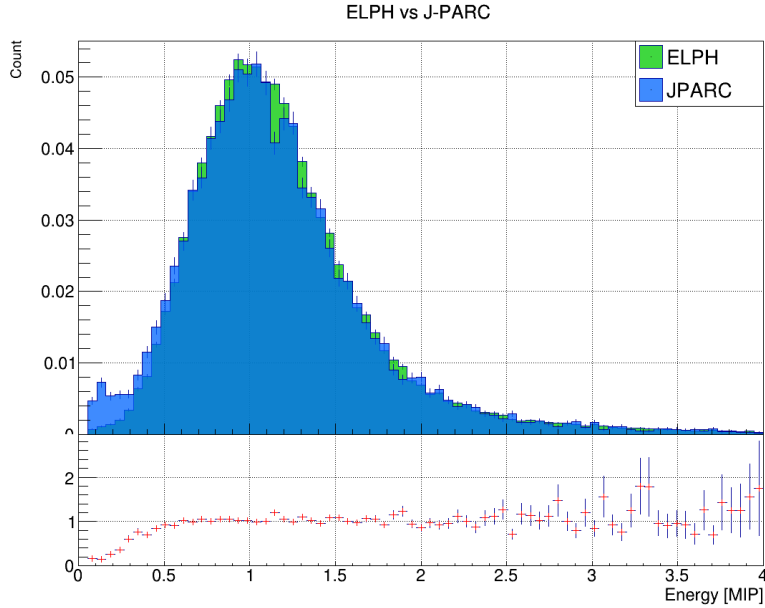


Figure 5.10: Energy distribution of events in ELPH compared to K^\pm .

5.5.2 Charged Kaon Selection criteria

To select events the same cut were made that were done in the 2016 to 2018 analysis [11]. The distribution of cut variables before the respective cuts were made are shown in Fig. 5.7, Fig. 5.9, and Fig. 5.8. Events are excluded if they have energy deposition in veto detectors other than CV. The location between the hits on CV and on CSI are required to match for π^\pm . The timing difference between the 2γ is required to be less than 3 ns and between the 2γ and the π^\pm less than 5 ns. The clusters' locations are required to be within the central $150 \text{ mm} \times 150 \text{ mm}$ square of CSI, known as the fiducial region. The clusters are required to be larger than 4(5) crystals for the $2\gamma(\pi^\pm)$. The angle in the xy -plane between the trajectory of the π^\pm and the reconstructed π^0 is required to be greater than 140° because the pions are emitted back to back. The π^0 transverse momentum is required to be greater than 80 MeV. The π^\pm energy measured in the calorimeter is required to be between 200 MeV and 400 MeV. Additionally a cut is made on the 2γ cluster shape.

5.5.3 Comparison to Electron Beam Data

Data was taken with the sweeping magnet turned off. This allows a large number of K^\pm that are generated upstream to flow into the detector providing a high-statistics data set. After K^\pm reconstruction, the energy distribution of remaining events was compared to that of ELPH as shown in Fig. 5.10. Both histograms are normalized to their respective entries and their peaks normalized to 1 MIP. Comparing the shape of the two, the higher energy region is consistent but there is a discrepancy in the number of events near the pedestal. These events may arise from a contamination of the sample, inefficiency in the UCV, or K_L passing outside the UCV. One possibility for contamination is from the decay of $K_L \rightarrow \pi^+\pi^-\pi^0$. The purity of this data set will be evaluated in the future. When calculating the inefficiency using K^\pm data this

discrepancy accounts for an additional 2% inefficiency. Whether this is true inefficiency or contamination of the data set is currently unclear. It is taken as true inefficiency for a conservative estimate in this thesis. The inefficiency after applying a threshold will be discussed in Section 6.2.

Chapter 6

Impact of Upstream Charged Veto

6.1 Accidental Loss

When evaluating the impact on the KOTO experiment, the threshold was chosen to vary as to maintain a constant accidental loss of 5%. As the dark current of the MPPCs increase the threshold will be increased as well to maintain the same accidental loss. This effect can be seen in Fig. 6.1a. Over the course of the spring 2021 run the dark current increased to a maximum of 5 μA . The total accidental loss during the spring 2021 run, evaluated without the effect of the UCV, was 58%. The total accidental loss including the effect from the UCV has not yet been evaluated but assuming a fixed accidental loss of 5%, the additional effect is expected to be 5% or less because of correlation between accidental losses in different detectors.

6.2 Background Reduction

The reduction of the K^+ background that the UCV can achieve is related to the inefficiency and therefore the threshold used for analysis. By applying the threshold calculated in Fig. 6.1a, the inefficiency was calculated at different values of dark current in the 2021 spring run. This changing inefficiency is shown in Fig. 6.1b. The maximum inefficiency occurred at the end of the run at 5 μA of dark current and was (3.99 ± 0.15) %.

As explained in Section 1.3 the expected charged kaon background in the 2016-2018 data set was 0.87 ± 0.25 events. With a similar data set the UCV would be able to reduce the background to 0.035 ± 0.01 events. This corresponds to 0.84 times the number of predicted events for $K_L \rightarrow \pi^0 \nu \bar{\nu}$ by the standard model. The UCV was used during all of the 2021 runs. The data collected in 2021 is equivalent in amount to the 2016-2018 data.

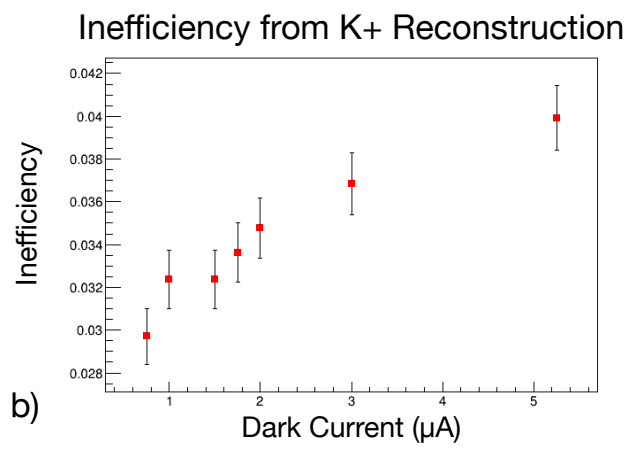
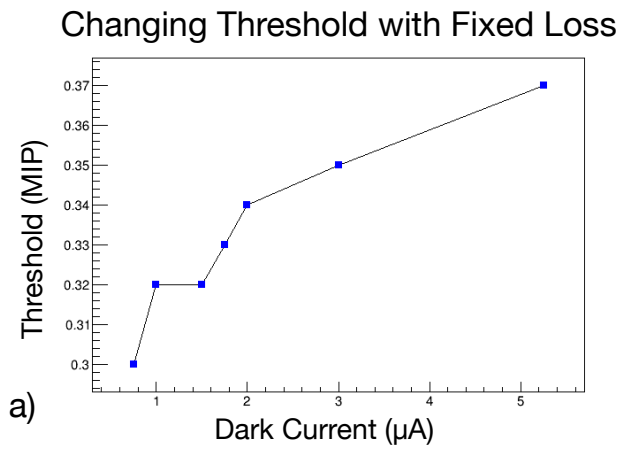


Figure 6.1: a) Threshold as a function of dark current to keep the accidental loss of UCV at 5% (a) and inefficiency of the UCV using the respective threshold (b).

Chapter 7

Discussion

7.1 Longevity of MPPCs

The UCV was designed to have replaceable MPPCs. Due to the large effect from irradiation and therefore the increase in accidental loss, ease of replacement was included in the design. Because the MPPCs are only attached to the front-end board by soldering and not attached to the MPPC holders, they can be easily removed by removing the circuit board and unsoldering them. After the spring run in 2021 and partway through the summer run in 2021 the MPPCs were replaced. The replacement took less than 24 hours and was therefore able to be completed during a maintenance day. After re-installation, the UCV continued to perform without any major issues. Replacement can be done again in the future if necessary.

7.2 Accidental Loss Calculation Method

Although the accidental loss was calculated as described in Section 4.5.1, the accidental loss can also be calculated from the rate. The rate is calculated in the following way,

$$R = \frac{\# \text{ total peaks}}{(\# \text{ total events}) \times (256 \text{ ns})},$$

where the number of total peaks are only counted if they cross a threshold. Because the number of peaks is discrete, the probability of having x hits in the UCV follows a Poisson distribution,

$$P(x; \lambda) = \frac{e^{-\lambda} \lambda^x}{x!},$$

where λ is the average number of hits calculated from the rate and the timing window as

$$\lambda = Rt.$$

Since the UCV is a veto detector, to veto signal we need to have 0 hits. Therefore the accidental loss is the probability of getting a hit count greater than 0,

$$\text{Accidental Loss} = P(x \geq 0; \lambda) \tag{7.1}$$

$$= 1 - P(x = 0; \lambda) \tag{7.2}$$

$$= 1 - e^{-\lambda}. \tag{7.3}$$

Because the accidental loss is calculated from the average rate, this method assumes that all hits are randomly distributed in time and across channels. If there are correlations between the hits, the resulting accidental loss will not accurately represent the effect on $K_L \rightarrow \pi^0 \nu \bar{\nu}$. This method was looked at for TMon and yielded a few percent larger accidental loss than the former method and was chosen not to be used.

Chapter 8

Conclusion

The KOTO experiment at J-PARC searches for the rare kaon decay $K_L \rightarrow \pi^0 \nu \bar{\nu}$ to test for CP violation at J-PARC. The ratio of K^\pm to K_L in the beam is $(2.6 \pm 0.1) \times 10^{-5}$ [2]. To veto these K^\pm , a charged particle detector was built and installed for placement in the beam upstream of the decay region. It was designed to have an inefficiency of less than 10% and to result in accidental loss $\mathcal{O}(5\%)$ or less. The UCV was designed with $0.5 \text{ mm} \times 0.5 \text{ mm}$ scintillation fibers and $3 \text{ mm} \times 3 \text{ mm}$ MPPCs to detect particles. It was designed to have a changeable angle to overcome inefficiency caused by gaps between the fibers and to optimize the inefficiency and accidental loss. The UCV was tested using an electron beam at Tohoku University to confirm the inefficiency and the performance. Furthermore, the accidental loss at J-PARC was simulated and the angle was set to 25° , with an expected accidental loss of 6% and an inefficiency of 5%. After installation at J-PARC the performance was measured. After the spring run in 2021 the UCV was able to reduce the charged kaon background by 96% while causing an accidental loss of 5%.

References

- [1] J. K. Ahn et al. “Search for $K_L \rightarrow \pi^0 \nu \bar{\nu}$ and $K_L \rightarrow \pi^0 X^0$ Decays at the J-PARC KOTO Experiment”. In: *Phys. Rev. Lett.* 122 (2 Jan. 2019), p. 021802. DOI: 10.1103/PhysRevLett.122.021802. URL: <https://link.aps.org/doi/10.1103/PhysRevLett.122.021802>.
- [2] J. K. Ahn et al. “Study of the $K_L \rightarrow \pi^0 \nu \bar{\nu}$ Decay at the J-PARC KOTO Experiment”. In: *Phys. Rev. Lett.* 126 (12 Mar. 2021), p. 121801. DOI: 10.1103/PhysRevLett.126.121801. URL: <https://link.aps.org/doi/10.1103/PhysRevLett.126.121801>.
- [3] *MPPC*. Hamamatsu. Apr. 2021. URL: https://www.hamamatsu.com/resources/pdf/ssd/mppc_kapd9008e.pdf.
- [4] *MPPC (Multi-Pixel Photon Counter)*. Hamamatsu. Aug. 2016. URL: https://www.hamamatsu.com/resources/pdf/ssd/s13360_series_kapd1052e.pdf.
- [5] Shoji Nagamiya. “Introduction to J-PARC”. In: *Progress of Theoretical and Experimental Physics* 2012.1 (Oct. 2012). 02B001. ISSN: 2050-3911. DOI: 10.1093/ptep/pts025. eprint: <https://academic.oup.com/ptep/article-pdf/2012/1/02B001/11590524/pts025.pdf>. URL: <https://doi.org/10.1093/ptep/pts025>.
- [6] D. Naito et al. “Development of a low-mass and high-efficiency charged-particle detector”. In: *Progress of Theoretical and Experimental Physics* 2016.2 (Feb. 2016). 023C01. ISSN: 2050-3911. DOI: 10.1093/ptep/ptv191. eprint: <https://academic.oup.com/ptep/article-pdf/2016/2/023C01/19301233/ptv191.pdf>. URL: <https://doi.org/10.1093/ptep/ptv191>.
- [7] Yuya Noichi. “Estimation and Rejection of $K_L \rightarrow 2\gamma$ Background in the J-PARC KOTO Experiment”. MA thesis. Osaka University, Feb. 2021.
- [8] *Plastic Scintillating Fibers*. Kuraray. 2014. URL: https://www.kuraray.com/uploads/5a717515df6f5/PR0150_psf01.pdf.
- [9] Andrei D. Sakharov. “SPECIAL ISSUE: Violation of CP in variance, C asymmetry, and baryon asymmetry of the universe”. In: *Soviet Physics Uspekhi* 34.5 (May 1991), pp. 392–393. DOI: 10.1070/PU1991v034n05ABEH002497.
- [10] K. Sato et al. “CsI calorimeter for the J-PARC KOTO experiment”. In: *Nuclear Instruments and Methods in Physics Research Section A: Accelerators, Spectrometers, Detectors and Associated Equipment* 982 (2020), p. 164527. ISSN: 0168-9002. DOI: <https://doi.org/10.1016/j.nima.2020.164527>. URL: <https://www.sciencedirect.com/science/article/pii/S0168900220309244>.

- [11] Satoshi Shinohara. “Study of the $K_L \rightarrow \pi^0 \nu \bar{\nu}$ Decay at the J-PARC KOTO Experiment”. PhD thesis. Kyoto University, June 2021.
- [12] Ryota Shiraishi. “J-PARC KOTO Development of Circuits for Signal Amplification and Waveform Shaping for the High-Rate Charged Particle Detector Used for the KOTO Experiment at J-PARC”. MA thesis. Osaka University, Feb. 2021.